Ore Geology Reviews 113 (2019) 103060

Contents lists available at ScienceDirect

Ore Geology Reviews

journal homepage: www.elsevier.com/locate/oregeorev

Geology and geochemistry of Gunung Subang gold deposit, Tanggeung, Cianjur, West Java, Indonesia

Xi-Yao Li[a,b], Zheng-Wei Zhang[a,*], Cheng-Quan Wu[a,*], Jin-Hong Xu[a,b], Zi-Ru Jin[a,b]

[a] State Key Laboratory of Ore Deposit Geochemistry, Institute of Geochemistry, Chinese Academy of Sciences, Guiyang 550081, China
[b] University of Chinese Academy of Sciences, Beijing 100049, China

ARTICLE INFO

Keywords:
Epithermal gold deposit
In-situ Pb isotope
Fluid inclusion
S-Pb isotope
West Java
Indonesia

ABSTRACT

The Gunung Subang gold deposit is located in the Sunda arc volcanic belt in West Java, Indonesia. The ore bodies are associated with volcanic rocks from the Miocene Koleberes and Bentang Formation. To constrain the significance of the ore genesis and mineralization, this study was carried out with the aim of examining the deposit using methods such as detailed field observation, petrography, petrochemistry, zircon U-Pb dating, Hf isotope, fluid inclusion analysis, and sulfur and in-situ Pb isotope analyses. The results suggest the following. (1) The volcanic rocks in Gunung Subang belong to the basalt-andesite group, with 48.66–79.17% (average 61.04%) SiO_2. The trace element patterns of the volcanic rocks exhibit relatively low HREE content, flat HREE patterns, and weak negative or positive Eu anomalies, which are similar to those of typical arc magmatic rocks. (2) Most zircons selected from the volcanic rocks are magmatic, and only a few are inherited. The magmatic zircons have a weighted mean U-Pb age of 17.0 ± 0.4 Ma, and the inherited zircons are from the Precambrian, dated at 887–2379 Ma. The magmatic zircons have $\varepsilon_{Hf}(t)$ values ranging from −1.24 to 13.59, indicating that the magmatism may be contaminated, predominantly with juvenile crust but also with a small percentage of ancient crust. (3) The sulfur isotopic compositions are fairly uniform, and the $\delta^{34}S$ values of pyrite, galena, and sphalerite range from 0.53 to 2.97‰, suggesting a magmatic origin. (4) The Pb isotopic compositions of pyrite and galena are clustered, and some include relatively high amounts of radiogenic lead. The mean ratios of $^{206}Pb/^{204}Pb$, $^{207}Pb/^{204}Pb$, and $^{208}Pb/^{204}Pb$ are 18.59 ± 0.007, 15.65 ± 0.007 and 38.89 ± 0.017, respectively, indicating that the ore-forming material is highly related to Miocene to Pliocene volcanic rocks. (5) Fluid inclusions in the quartz from the ores are liquid and vapor-liquid phases, with components of the NaCl-H_2O system with homogenization temperatures of 240–320 °C and salinities of 0.2–6.2 wt% NaCl. The coexistence of vapor and liquid-rich fluid inclusions suggests that boiling occurred throughout the deposition of the ore. (6) The results of Electron Probe Microanalysis (EPMA) indicate that pyrite is the major Au-bearing mineral. Combined with the observation of scanning electron microscope (SEM), gold is primarily present as Au-Ag-telluride minerals, and there may also be native gold (Au^0). Finally, we consider the Gunung Subang is an epithermal gold deposit related to the Mid-Miocene magmatism.

1. Introduction

Java Island is endowed with a number of epithermal gold deposits and porphyry deposits, owing to the geological setting of the Sunda Arc which was formed by the subduction of the Indian-Australia Plate beneath the Eurasian Plate (Setijadji et al., 2006). In West Java, there are two distinctive Cenozoic magmatic belts that become younger from the south to the north. The younger is the Late Miocene-Pliocene magmatic belt (12 to 2 Ma), and the older is the Late Eocene-Early Miocene magmatic belt (40 to 18 Ma) (Fig. 1b) (Hall, 2007; Soeria et al., 1994). In the Bayah Dome, low-sulfidation epithermal Au-Ag deposits with a mineralization age from the Pliocene-Pleistocene, have historically been mined and are known for the presence of substantial resources, including Pongkor (Milési et al., 1999; c), Cikidang (Rosana and Matsueda, 2002), and Cirotan (Genna et al., 1996). As for the Late Eocene-Early Miocene magmatic belt, several gold prospects with Miocene mineralization have been explored, including the Cijulang (Myo et al., 2014), the Arinem Te-bearing Au-Ag metal deposit (Yuningsih et al., 2012), and the Ciemas deposit (Wu et al., 2014; Zhang et al., 2015). The ore deposits in the older magmatic rock belt can be classified into low-sulfidation (Basuki et al., 1994; Sudana and Santosa, 1992; Angeles et al., 2002; Rosana and Matsueda, 2002), high-

* Corresponding authors.
E-mail addresses: zhangzhengwei@vip.gyig.ac.cn (Z.-W. Zhang), wuchengquan@mail.gyig.ac.cn (C.-Q. Wu).

https://doi.org/10.1016/j.oregeorev.2019.103060
Received 31 March 2019; Received in revised form 15 July 2019; Accepted 2 August 2019
Available online 07 August 2019

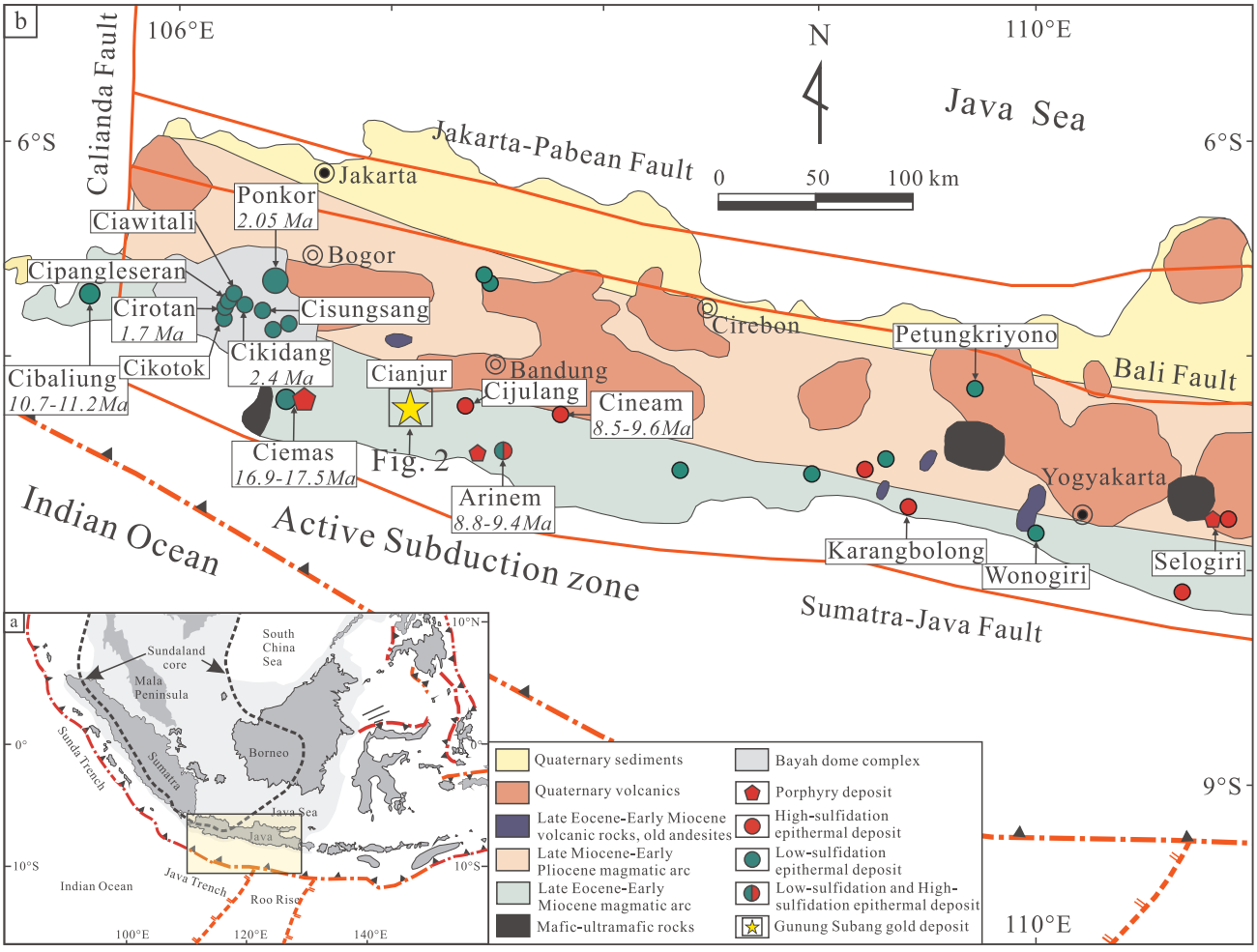

Fig. 1. Sketch of a geological map of West Java, Indonesia. (a) Map of Tectonic locations. (modified after Hall, 2002; Hall et al., 2008); (b) Distribution of regional geology and gold deposits in West Java (modified after Milési et al., 1994; Yuningsih et al., 2012; Zhang, et al., 2015).

sulfidation (Myo et al., 2014; Widi and Matsueda, 1998), and low-sulfidation overprinted with high-sulfidation (Yuningsih et al., 2012), with mineralization ages that are concentrated in the Middle to Late Miocene. Therefore, Java is an ideal area to study arc magmatism and the related porphyry-epithermal metallogenic mineralization (Marcoux and Milési 1994; Zhang et al., 2015).

The porphyry-epithermal metallogenic systems in Java have distinct temporal and spatial zonation (Fig. 1b) (Wu et al., 2019). Low-sulfidation and a minimal number of porphyry deposits tends to be concentrated in West Java (Marcoux and Milési 1994; Zhang et al., 2015), while high-sulfidation and abundant porphyry deposits are found in East Java (Maryono et al., 2018). Detailed research has been conducted on the Pliocene to Pleistocene deposits in Bayah Dome, West Java, such as the Pongkor Au-Ag (Milési et al., 1999; Basuki et al., 1994), the Cikidang Au-Ag (Rosana and Matsueda, 2002), and Cirotan Au deposits (Genna et al., 1996). In previous research, the oldest epithermal deposit in West Java is the low-sulfidation Cibaliung Au-Ag deposit (11.18–10.65 Ma) (Sudana and Santosa, 1992). However, the discovery of Ciemas (Wu et al., 2014; Zhang et al., 2015; Zheng et al., 2017) and Gunung Subang, which are both Mid-Miocene (~17 Ma) Au deposits, has advanced the previous understanding of mineralization in West Java.

The Gunung Subang deposit is located in Tanggeung, in the southern part of Cianjur District, West Java, Indonesia (Fig. 1a). Exploration has been carried out by the Director of Mineral Resources Inventory (DMRI) in cooperation with PT Aneka Tambang under the assistance of France and PT Sangga Buana Minerals. Since 2003, Lee and Kim (2003) and Ismayanto et al. (2009) have conducted mineralogical and geochemical studies, and have suggested that the genesis of the deposit is closely related to the magmatic hydrothermal activity whereby Tertiary andesite and dacites was intruded into the sediments, from the perspective of the formation of ore in space and time. The gold- and base-metal mineralization were formed by local boiling throughout the deposition of the ore, and are associated with an NNE-SSW trending quartz vein, However, the source of the mineralization-related magmatism and the occurrence of gold are still not well-known. To better constrain the ore genesis of the Gunung Subang gold deposit and to further understand that of the epithermal gold deposits in West Java, we conducted experiments concerning the major and trace elements, U-Pb age, the Hf isotopes, the S isotopes, the in-situ Pb isotopes, fluid inclusions, and electron probe microanalysis.

2. Geological background

The Gunung Subang gold deposit is situated within West Java at the southern margin of Sundaland which is the continental core of Southeast Asia and was formed by the accretion of blocks at the Eurasian margin at the Late Triassic (Fig. 1) (Hall, 2002). The Sunda-Banda arc (Fig. 1b) is a typical convergent plate margin that was developed along the northern margin of the Indian-Australian plate subduction following the collision with the Eurasian Plate that occurred during the Cenozoic (Carlile and Mitchell, 1994), creating an active continental margin magmatic belt. During the Early Miocene, an important episode of volcanism took place in south Java as a result of the

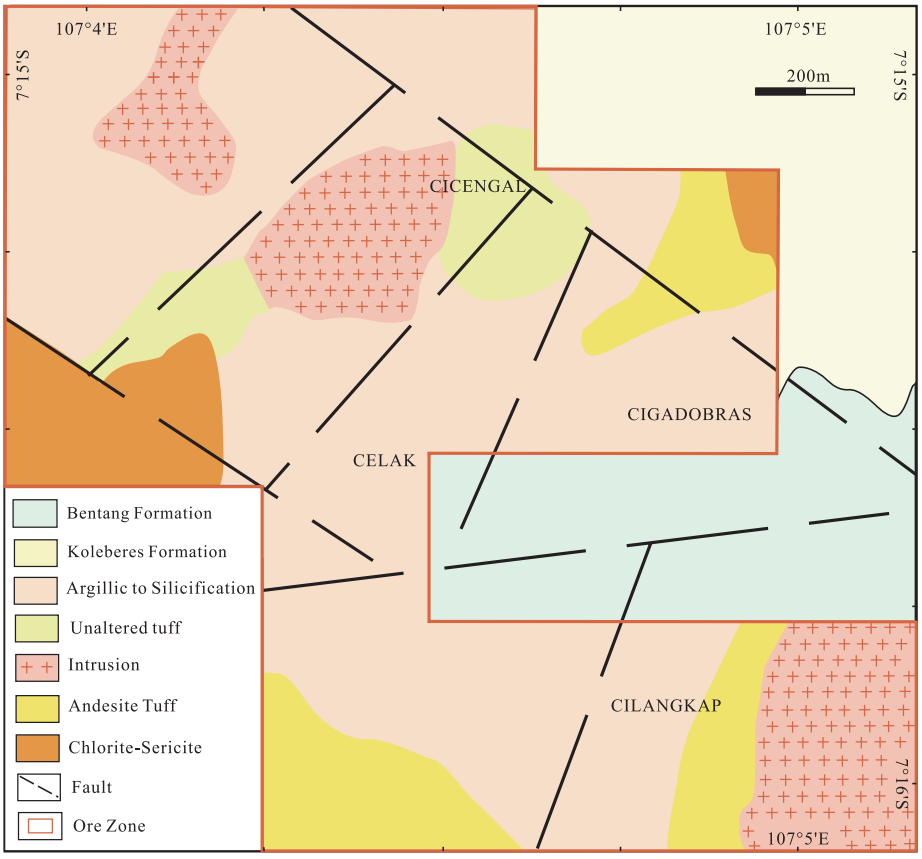

Fig. 2. Simplified geological map of the Gunung Subang area showing the location of the four veins of the deposit (modified after Widjaja, 2017).

Table 1
Sedimentary lithostratigraphy of the host rocks for the Au-Ag polymetallic deposits in the Gunung Subang area, West Java, Indonesia (modified after Ismayanto et al., 2009; Widjaja, 2017).

	Formation	Member	Lithological description
Miocene	Koleberes		Late Miocene in age, consists of well bedded, poorly consolidated tuff sandstone and crystal tuff with intercalation of tuff, pumiceous tuff breccia and breccia. Grey or brownish-grey sandstone consists mainly of andesitic rock fragments with subordinate pumice.
	Bentang		Miocene in age, consists of alternated tubidites comprising well bedded, poorly consolidated tuff sandstone, crystal tuff and pumiceous tuff with intercalations of globigerina claystone, siltstone, marly clay, and lentills of andesitic breccia, conglomerate, lapilli tuff, and tuff breccia. In the upper sequence, claystone and siltstone predominate. Pumice breccia contains rock fragments as much as 5 cm in diameter.
		Kadupandak	Late Miocene in age, consists of plastic claystone, siltstone and tuffaceous claystone, usually grey to black, locally greenish. Intercalations of alternating pumiceous tuff, lapilli and andesite breccia.

northward subduction of the Indian-Australia Plate beneath the Eurasian Plate, which led to the development of a system of calderas (Fig. 1) (Hall, 2007). Andesite and other plutons were generated in sequence. Faults and fractures became important sites as channels or spaces for the deposit of subsequent mineralization (Zhang et al., 2015).

The Sumatran-Java trench lies in a NW-EW direction, with a total length of over 4880 km (Fig. 1a) (Hamilton, 1979). The faults in Java mainly trend to the EW and NS, including the middle segment of the Sumatra- Java fault, the western segment of the Bari fault, and the southern segment of the Calianda fault (Fig. 1b) (Hamilton, 1979). The regional structure in Gunung Subang has two sets of main fault orientations: the NW strike and near E-W strike (Fig. 2).

The exposed strata in Java were predominantly formed during the Tertiary and Quaternary (Fig. 1b) (Hamilton, 1979). Tertiary and Quaternary pyroclastic rocks are mainly distributed in south and central Java. These are mainly rhyolitic, dacitic-andesitic tuff, breccia, and lava, and are partially intercalated with sandstone, shale, carbonaceous tuff and mudstone. In northern Java, the Quaternary sediments are dominant (Fig. 1b) (Hamilton, 1979; Wakita and Metcalfe, 2005).

The magmatism that occurred in Java was mainly during the Cenozoic (Katili, 1974). Java Island contains two distinctive Cenozoic magmatic belts (Fig. 1a) (Hall, 2007; Soreia et al., 1994) and the Quaternary volcanic rocks are located in north-central Java (Fig. 1b) (Nicholls et al., 1980; Soreia et al., 1994). Gunung Subang is located within the late Eocene-early Miocene belt (Fig. 1b), with a number of andesites that extend over several kilometers (Fig. 2).

3. Deposit descriptions

Gunung Subang is associated with magmatic events that occurred in the Mid-Miocene. The ore zone is dominated by sediments from the Paleogene to the Neogene age in the west and from the Paleogene to the Quaternary in the east (Table 1). The Tertiary volcanic rocks include breccia, tuff, and andesite. The Quaternary volcanic rocks consist of a variety of andesitic rocks, alluvial, and residual deposits (Fig. 2).

Volcanic tuff covers more than 65% of the area, which is characterized by tuff, lapilli-tuff, breccia-tuff, reddish brown light grey to pale green and medium to highly weathered (oxide), andesitic-dioritic fragments, medium-highly fractured. This lithology unit has intense argillic and silicified alteration, with slightly prophylitic (chlorite)

Table 2
General characteristics of the mineralized veins in the Gunung Subang area (after Ismayanto et al., 2009; Widjaja, 2017).

Vein Name	Strike/Dip	Width (m)	Major minerals	Alteration	Au (ppm)	Ag (ppm)	Cu (ppm)	Pb (ppm)	Zn (ppm)
Cilangkap	N 5°E/80° E	0.01–0.05	Pyrite-chalcopyrite, calcite and quartz	intensive argillic, weakly porphyritic	0.22	10.70	19800.00	2226.00	498.21
Celak	N 29°E/77° SE, N 0°E/81° E, N 355°E/80° E, N20°E/71° SE, N205°E/30° NW, N300°E/40° NE	0.01–0.2	hematite, sphalerite/galena, pyrite, malachite	medium-intense argillic, slightly prophylitic, silicification	0.08	21.40	34515.00	1794.00	7335.00
Cigodobras	N235°E/65°, N15°E/69°, N210°E/68°, N350°E/75°, N190°E/75°	0.01–0.2	Pyrite, sphalerite/galena	argillic and silicified	14.49	17.00	8.25	107.68	35.36
Cicengal	N24°E/74°	0.01–0.05	Pyrite	Silicification	–	–	–	–	–

alteration which is spotted over small areas. Tuff as host rock is located in Cicelak, Cigadobras, Cibogo (Table 2). The tuff unit is equivalent to the Late Miocene Koleberes Formation. Andesite with a gray color and porphyritic texture covers the center north area, the SE region, and the SW area, namely the Cilangkap and Celak areas. Andesite has intruded into the Bentang and Koleberes Formation, and can be divided into three major modes of occurrence within the district: boulder type andesite with an onion structure in the soil, massive type andesite, and andesite with well-developed sheeting structure (Kim et al., 2002). These structures consist of randomly oriented orthopyroxene, clinopyroxene, plagioclase, and matrix that is predominantly composed of plagioclase (Fig. 5h). The ore mineralization in the district is likely to be associated with andesite (Fig. 2) (Ismayanto et al., 2009; Lee and Kim, 2003; Widjaja, 2017).

Four ore blocks have been discovered (Fig. 2), known as Cicengal, Cicadobras, Celak and Cilangkap. The inferred Au resources are 50 t with 0.5 to 2 ppm grade (Ismayanto et al., 2009; Lee and Kim, 2003; Widjaja, 2017). The most promising prospect is Celak and the samples were therefore taken from this block. The exposed ore body is 6 m thick and is extended over 1–2 km (Widjaja, 2017). The two ore types in Celak have been identified as quartz-sulfide veins and tuff breccia. These orebodies are hosted within the relatively well explored Bentang Formation in the Jampang Dome complex of the West Java Neogene Magmatic Arc (Ismayanto et al., 2009; Lee and Kim, 2003; Widjaja, 2017).

Regional mapping suggests that the main local geological structures have similar trends with W-E and NW-SE dextral strike slip faults at the prospect scale. Brittle structures which are generally trending north to the NE and WE and are found in the west tend to be obscured by Quaternary volcanic cover. The secondary structure, which runs NNE-SSW, trends perpendicularly with the main structures. This structure is believed to be associated with mineralization (Ismayanto et al., 2009; Lee and Kim, 2003; Widjaja, 2017).

The textures of the ores include euhedral-subhedral granular (Fig. 5a–d), xenomorphic fine to micro-grand granular, and columnar and pyrite framboid (Fig. 5k). The ore structures are mainly disseminated, brecciated, comb, radiated, veinlet, and massive. The types of alteration mainly consist of silicification, argillic alteration, and some prophylitic alteration covering lilted areas (Figs. 2 and 3). The presence of comb structures and drusy structures (Figs. 4e, g and 5e, g) indicate the open-space filling of the near-surface environment. The open-space filling, chalcedonic quartz and breccias are common in the study area, and they are distinct features of epithermal ore deposits (Chen et al., 2011).

Metal minerals are predominantly Au-Ag telluride, Se-bearing minerals, tetrahedrite, pyrite, sphalerite, and galena (Figs. 4–6). Au-Ag telluride minerals include krennerite and hessite, of size 3–10 μm. Se-bearing mineral is kurilite–$(Ag, Au)_2(Te, Se, S)$, with grains of size 1–3 μm, which is mainly distributed within the fractures of the quartz, pyrite, or chalcopyrite crystals, some of which were warped by these minerals. Krennerite and some hessite formed in the early often occur in the form of subhedral mosaic intercessions. Gangue minerals in the formation are mainly quartz, sericite, and illite. Gold-rich tellurides preceded the formation of silver-rich tellurides. Pyrite, one of the dominant sulfides, is ubiquitous in the form of fine to coarse crystalline aggregate. The pyrite veins crosscut the chalcedony (Fig. 4b) and have a close relationship with gold mineralization. Euhedral to subhedral pyrite are commonly disseminated in the pyrite veins. Fine euhedral grains are commonly disseminated in the host rocks. Highly brecciated fragments of pyrite are commonly cemented with chalcopyrite and galena. Chalcopyrite, the most dominant copper mineral in the veins, mainly occurs in the form of irregularly shaped masses and as medium to fine-grained disseminates, and can also be found as anhedral grains that have intergrown with pyrite and sphalerite. Sphalerite usually occurs as anhedral masses throughout the veins and is closely intergrown with chalcopyrite and galena. Bornite occurs mostly as an

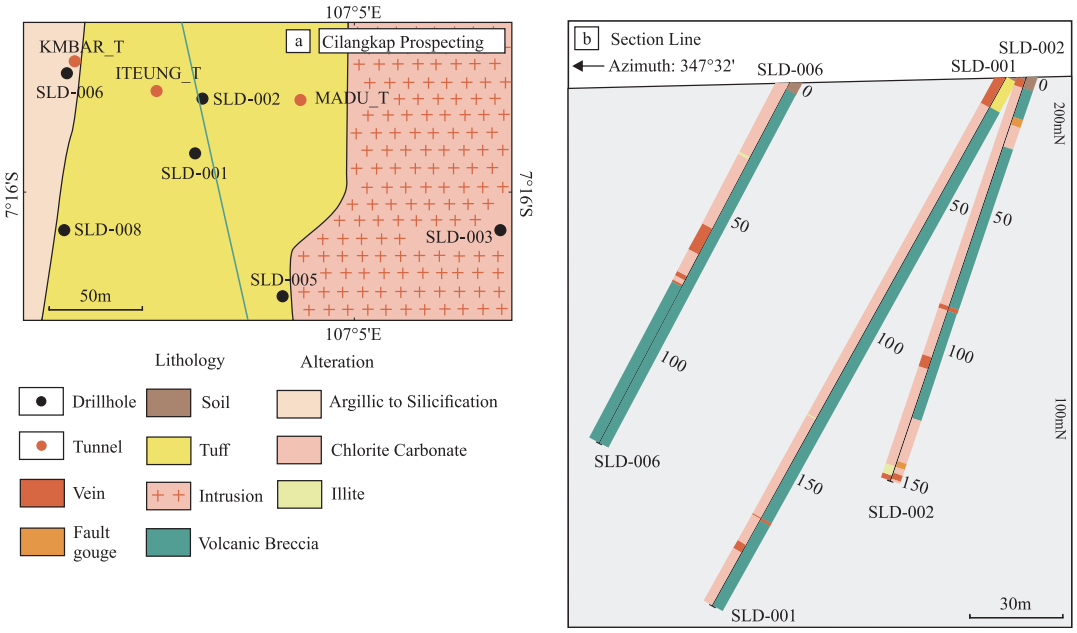

Fig. 3. (a) Geological map of the prospecting line of the Cilangkap vein in the Gunung Subang deposit. (b) a cross-section of the Line (modified after Widjaja, 2017).

Fig. 4. Photos of orebody outcrops, hydrothermal alteration, and mineralization at the Gunung Subang deposit. (a) Ore bodies, in an exposed andesite and argillaceous zone. (b) Accretionary lapilli tuff. (c) Ore body in a quartz zone. (d) Quartz vein type ore. (e) Quartz vein type ore. (f) Andesite wall rock. (g) Colloform quartz with disseminated pyrite. (h) Breccia type ore. (i) Quartz-sulfide vein, with disseminated pyrite.

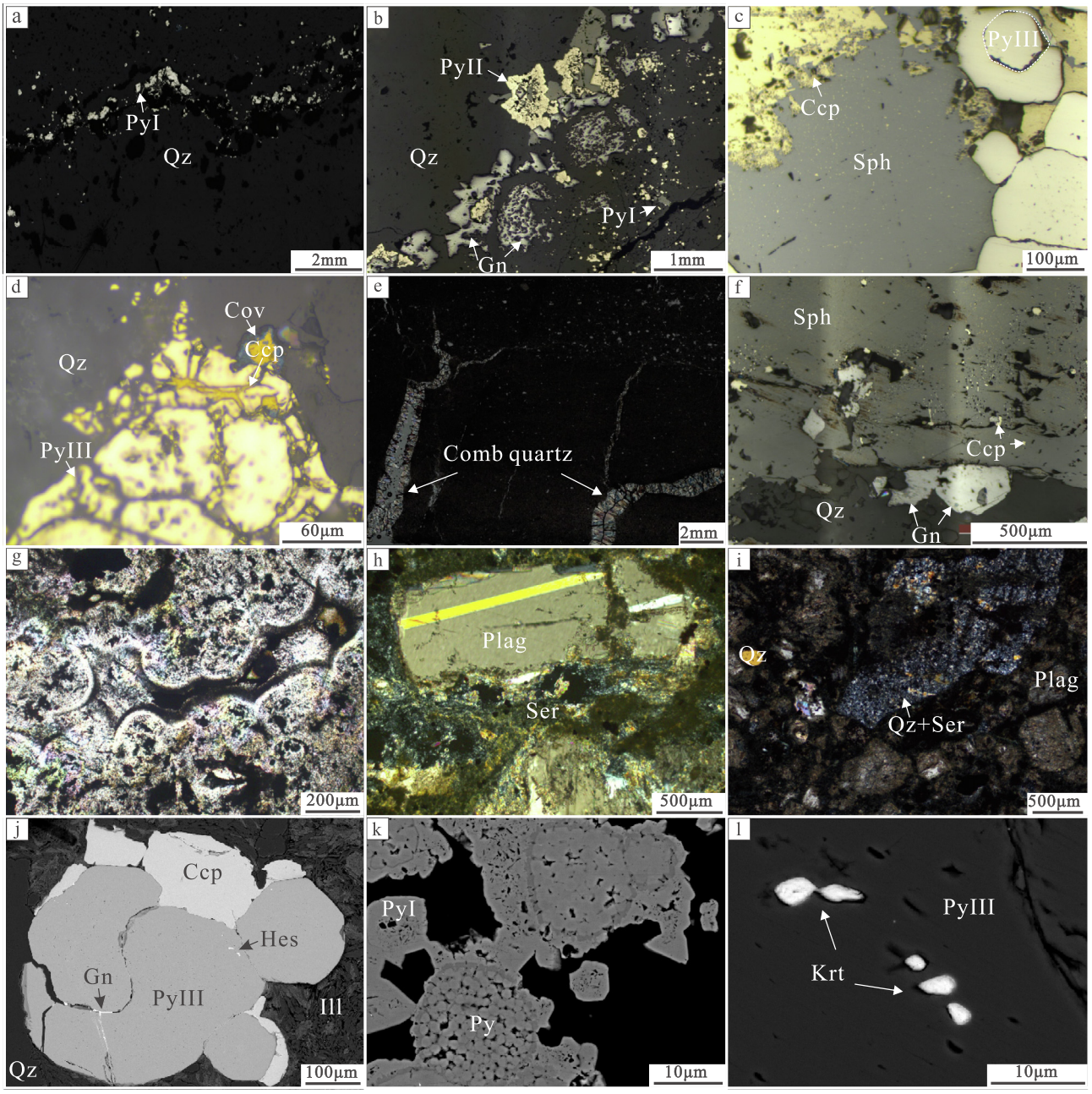

Fig. 5. Photomicrographs and BSE images of ore mineralogy showing PyI to PyIII, Hes, Krt, Ccp, Sph, Gn, and Cov. (a) Disseminated euhedral-subhedral pyrite in a quartz matrix. (b) Disseminated euhedral-subhedral pyrite coexisting with sphalerite and recrystallized galena. (c) Sphalerite exsolved with chalcopyrite is intergrown with PyIII. (d) Py with veined chalcopyrite, some chalcopyrite has been oxided into covellite. (e) Comb quartz in chalcedony. (f) Sphalerite exsolved with chalcopyrite is intergrown with galena. (g) Drusy cavity enclosed by quartz, showing open-space filling. (h) Plagioclase phenocrysts rimed with sericitic alteration in altered basalt andesitic host rocks. (i) Plagioclase phenocrysts replaced by chlorite in argillic alteration and alteration via silicification in altered basalt. (j) Hessite is surrounded by pyriteIII, with illite and quartz. (k) Framboidal pyrite in quartz vein ore. (l) Subhedral krennerite in PyIII. A-f, h-i are under cross polarized light; g is under plane polarized light; j-l are BSE images. Mineral abbreviations: Hes-hessite, Krt-krennerite, Py-pyrite, Ccp-chalcopyrite, Sph-sphalerite, Gn-galena, Cov-covellite, Plag-plagioclase, Ser-sericite, Qz-quartz.

intermediate alteration phase of chalcopyrite, and may occur within the original chalcopyrite. Goethite and covellite occur as alteration products, of which goethite primarily replaces hematite and galena and covellite mainly replaces grains in the margins of the chalcopyrite.

Three paragenetic stages (Fig. 6) are recognized in the mineralization of the Gunung Subang deposit, based on crosscutting relationships and mineral assemblages: Illite, sericite, and chlorite (stage I), gold-bearing pyrite-quartz veins (stage II), and hematite-covellite-goethite veins (stage III). Stage II is the major period during which gold is precipitated.

According to petrographic observation and the content of Au and Ag, the pyrite can be divided into three periods with the following characteristics:

(1) PyI: Euhedral pyrite, mainly distributed in silicified ore, with nonuniform sizes at μm level and smooth surfaces, in the form of a square under the microscope (Fig. 5a).
(2) PyII: Subhedral-euhedral pyrite, generally distributed in silicified ore and fractures (Fig. 5b). These vary in size, from μm to mm level. The crystals are a little cracked, with a rough surface and a zigzag

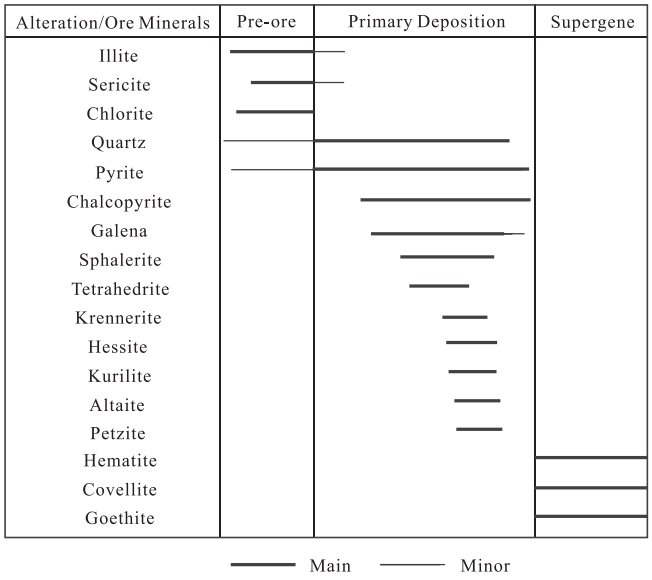

Fig. 6. Generalized paragenetic sequence of alteration and ore minerals (modified after Lee and Kim, 2003).

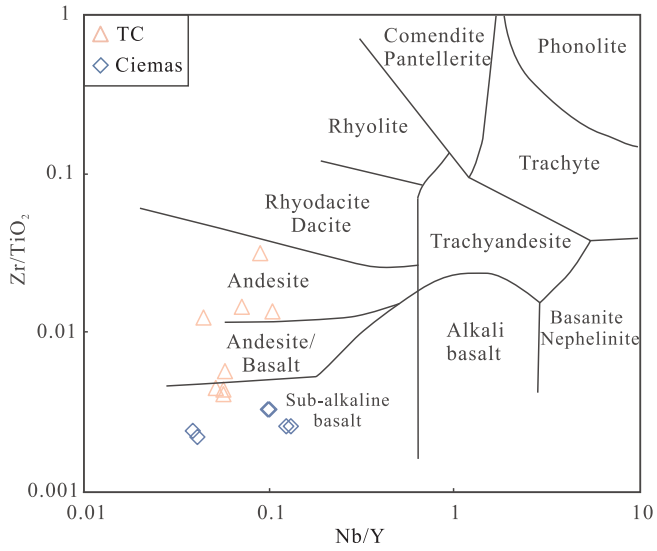

Fig. 7. The chemical classification and nomenclature of volcanic rocks using the Zr/TiO_2 vs. Nb/Y diagram (Winchester and Floyd, 1977). Ciemas data Source: Wu et al., 2014.

margin, suggesting compression. Some have a gridle structure.

(3) PyIII: Euhedral pyrite, mainly distributed in silicified ore, of non-uniform mm level sizes and with a smooth surface, most in the form of a square or a hexagon under the microscope. Fig. 5c shows two generations of euhedral pyrite.

(4) Framboidal pyrite: framboidal structure (Fig. 5k), generally aggregated. Monomer is small (radius < 10 μm) and round, composed of minor pyrite particles (usually of several μm). Its range of distribution is relatively small.

4. Sampling and analytical methods

Twenty-eight samples were collected from the quartz-sulfide veins and the wall-rock from the volcanic areas in Celak prospect. The whole rock abundance of the major elements was analyzed using X-ray fluorescence (XRF), U-Pb isotope analysis of zircon, sulfur isotope analysis, in-situ Hf isotopic ratio analysis of zircons, fluid inclusion study, and EPMA, which were conducted at the State Key Laboratory of Ore Deposit Geochemistry, Chinese Academy of Sciences. The in-situ Pb isotope analysis were conducted at the State Key Laboratory of continental Dynamics, Northwest University, Xi'an.

All volcanic samples were crushed to 200 mesh for whole-rock geochemical analysis, including major and trace elements. Trace elements were analyzed with inductively coupled plasma mass spectrometry (ICP-MS). The methods used for all analyses are shown in Qi et al. (2000).

U-Pb isotope analysis of the zircon was conducted by LA-ICP-MS, using a GeoLasPro laser ablation system (Lambda Physik, Gottingen, Germany) and an Agilent 7700x ICP-MS (Agilent Technologies, Tokyo, Japan). The 193-nm ArF excimer laser was focused on the zircon surfaces with an energy intensity of 10 J/cm^2. The ablation protocol employed a spot diameter of 32 μm with a 5 Hz repetition rate for 40 s (equaling 200 pulses), transported to the ICP-MS by helium. Zircon 91,500 was used as an external standard and zircon PL (with resultant ages of 5.6 ± 0.9 Ma and 4.8 ± 0.7 Ma) and QH (with a resultant age of 162 ± 3.1 Ma) were treated as quality controls for the geochronology. The abundance of lead in the zircons was externally calibrated against NIST SRM 610 with Si as an internal standard, and Zr was used as an internal standard for other trace elements. The resultant ages and isotopic ratios of these standards were reliable and reproducible, and yielded good agreement with the reference (Hu et al., 2011; Li et al., 2013; Liu et al., 2009). Raw data reduction was performed off-line using ICPMSDataCal software (Liu et al., 2009; Liu et al., 2010). The method used for common lead correction is shown in Andersen (2002). The concordia diagrams and calculations of the weighted average ages were performed with Isoplot/Ex-ver2 (Ludwig, 2003).

Sulfur isotope analysis was conducted with a MAT253 Stable isotope mass spectrometer produced by Thermo Fisher Scientific (USA). Sulfide grains were crushed to 40–60 meshes and were handpicked under a binocular microscope for S isotope analysis. GBW 04415 and GBW 04414 are also determined as the standards. Analytical uncertainties for $\delta^{34}S$ are better than 0.1‰ (2σ).

In-situ Pb isotope analysis was conducted using a RESOlution M-50 laser ablation system (ASI, Australia), connected to a Nu Plasma II MC-ICP-MS from Nu Instruments (Wrexham, UK) at the State Key Laboratory of Continental Dynamics, Northwest University, Xi'an. Helium was used as the carrier gas with an uptake rate of 280 mL/min, a repetition time of 6 Hz, and an energy density of 6 J/cm^2 during the laser ablation process. The diameter of the laser ablation beam was 9 μm for galena and 100 μm for other sulfides. Each analysis consisted of a background measurement for 30 s, followed by 50 s of ablation for signal collection and an additional 40 s of washing time. The PSPT-2, Gn01, and NIST SRM 610 glass served as internal and external standards, respectively. The measured isotopic ratios of the standards were highly reliable and reproducible and yielded good agreement with the references during the analytical process (Yuan et al., 2018). The details of the fs LA-ICP-MS in-situ Pb isotope analysis and instrument parameters are available in Bao et al. (2017).

Experiments for the in situ Hf isotopic ratio analysis of zircons were conducted using a Neptune Plus MC-ICP-MS in combination with a Geolas HD excimer ArF laser ablation system. Helium was used as the carrier gas within the ablation cell and was merged with argon (makeup gas) after ablation. Small amounts of nitrogen were added to the argon as makeup gas flow to improve the of sensitivity of the Hf isotopes (Hu et al., 2012a,b). All data acquired from the zircons was in single spot ablation mode with a spot size of 40 μm and an energy density of 6.0 J/cm. Each measurement consisted of 20 s for the acquisition of a background signal followed by 40 s for the acquisition of the ablation signal. Details of the operating conditions for the laser ablation system and the MC-ICP-MS instrument and analytical method are available in Hu et al. (2012a). Off-line selection and integration of analyte signals and mass bias calibrations were performed by ICPMSDataCal (Liu et al., 2009).

Fluid inclusion study is an important method that is used to understand the conditions and origins of the hydrothermal fluid. The

Table 3
Major (%) and trace element (10^{-6}) compositions of altered volcanics in Gunung Subang deposit.

Sample No. Sample type	TC-1 Andesite	TC-2 Andesite	TC-3 Andesite	TC-4 Basalt	TC-5 Basalt	TC-6 Basalt	TC-7 Andesite	TC-9 Andesite
SiO_2	49.69	70.85	75.74	41.63	43.70	41.30	56.35	59.40
Al_2O_3	17.22	13.36	12.26	16.21	16.10	17.39	15.15	14.98
Fe_2O_3	8.39	3.90	2.32	8.47	8.41	7.69	6.10	4.93
MgO	5.12	0.65	1.38	4.02	3.97	3.80	3.50	2.32
CaO	3.46	0.17	0.17	9.51	8.43	9.34	4.64	4.48
Na_2O	0.14	0.05	0.02	0.16	0.14	0.16	0.30	0.56
K_2O	4.18	3.51	3.21	3.17	3.02	3.54	2.24	2.46
MnO	0.23	0.02	0.10	0.15	0.14	0.15	0.10	0.08
P_2O_5	0.055	0.017	0.014	0.060	0.057	0.060	0.028	0.026
Ti	0.64	0.47	0.23	0.69	0.69	0.71	0.50	0.43
LOI	9.97	6.08	4.76	14.83	14.12	14.77	10.50	9.92
Li	20.9	5.95	15.7	14.2	14.1	12.4	18.5	14.7
Be	0.68	0.50	0.67	0.72	0.72	0.81	0.99	0.74
Sc	27.1	12.6	9.62	26.7	25.9	27.1	18.4	16.5
V	203	90.9	60.6	178	188	180	122	103
Cr	38.6	131	63.4	39.9	32.4	27.9	61.2	71.1
Co	16.5	9.30	5.20	17.9	15.9	13.6	12.6	9.90
Ni	6.40	4.80	3.70	8.50	7.80	8.20	8.0	6.40
Cu	85.2	57.3	11.2	64.1	58.2	62.8	18.7	72.1
Zn	96.8	60.5	109	91.5	107	101	106	54.8
Ga	17.7	12.5	9.00	16.9	16.6	20.1	15.8	15.2
Ge	1.0	0.66	0.48	1.10	1.10	1.05	0.91	0.79
As	4.70	10.1	7.50	3.70	4.70	3.40	3.30	3.10
Rb	79.9	63.9	56.9	63.7	60.4	71.0	48.1	52.5
Sr	63.4	7.30	56.0	57.4	46.1	75.4	37.4	36.9
Y	25.2	18.2	21.9	23.9	23.1	26.3	41.8	24.8
Zr	61.0	107	120	47.1	50.5	52.8	105	104
Nb	1.50	1.90	2.0	1.40	1.30	1.40	1.90	1.80
Mo	2.71	10.7	5.47	2.67	3.66	1.63	4.68	5.05
Ag	0.24	1.08	0.21	0.21	0.87	0.53	0.12	0.17
Cd	0.07	0.15	0.37	0.11	0.23	0.24	0.05	0.09
In	0.06	0.04	0.04	0.06	0.06	0.07	0.06	0.05
Sn	0.60	0.90	0.90	0.80	0.80	1.10	1.20	1.20
Sb	2.06	2.68	4.56	1.13	1.18	1.09	1.31	1.33
Cs	2.53	5.09	1.88	4.73	4.59	5.31	3.44	4.22
Ba	474	137	394	130	92.6	154	112	122
La	6.60	4.50	9.70	6.40	5.60	11.6	13.8	6.7 0
Ce	16.2	12.8	19.4	15.5	15.0	30.5	21.6	19.1
Pr	1.86	1.42	1.97	1.82	1.76	3.56	3.97	2.18
Nd	9.15	6.60	8.54	9.17	8.71	16.9	18.6	10.1
Sm	2.61	1.70	2.25	2.86	2.64	4.62	5.22	2.83
Eu	0.851	0.357	0.500	1.10	1.00	2.17	1.38	0.76
Gd	3.11	1.58	2.17	3.31	3.00	4.61	5.49	2.92
Tb	0.57	0.34	0.43	0.59	0.53	0.75	0.97	0.54
Dy	4.00	2.68	3.31	4.05	3.67	4.68	6.52	3.84
Ho	0.87	0.67	0.79	0.86	0.80	0.93	1.34	0.85
Er	2.50	2.14	2.45	2.36	2.18	2.36	3.66	2.51
Tm	0.38	0.36	0.41	0.35	0.34	0.34	0.57	0.40
Yb	2.47	2.53	2.83	2.27	2.23	2.12	3.69	2.71
Lu	0.39	0.41	0.45	0.35	0.33	0.30	0.54	0.42
Hf	1.80	3.10	3.40	1.40	1.40	1.50	2.90	2.80
Ta	0.11	0.14	0.16	0.09	0.10	0.10	0.15	0.14
W	1.0	0.70	0.50	0.60	0.60	0.70	0.60	0.50
Tl	0.87	0.68	0.67	0.60	0.55	0.62	0.40	0.41
Pb	9.30	434	94.3	6.90	5.90	5.40	6.10	4.90
Bi	0.07	0.19	0.11	0.08	0.08	0.09	0.23	0.20
Th	1.10	2.20	2.50	0.90	0.80	0.90	1.90	1.70
U	0.40	0.60	0.70	0.30	0.30	0.30	0.60	0.50

Note: LOI = loss on ignition.

microthermometry was performed using a Linkam THMSG 600 Hot & Cold Stage attached to a Leica DM2500 Microscope with temperatures that ranged from −196 °C to 600 °C. The uncertainties of the temperature measurements were ± 0.2 °C for < -70 °C, ± 1 °C for < 100 °C, and ± 2 °C for < 400 °C. The heating/freezing rate was set at 10–20 °C/min during the initial runs, and was reduced to 0.1 °C/min when near phase transformation. Raman spectroscopy for the vapor phase of individual fluid inclusions was measured with a Renishaw InVia Reflex Raman spectroscope. Excitation was provided using a Spectra-Physics argon-ion laser at 20 mW with a wavelength of 514.5 nm focused on a spot size of 1–2 μm, over a time period of 60 s or 180 s and a scope of 150–4000 cm^{-1}. For liquid-rich two-phase inclusions, the homogenization temperatures (Th) were measured by heating the inclusions to the liquid phase (Bakker and Jansen, 1994; Lu et al., 2004). The salinities of the liquid-rich fluid inclusions were calculated from the last ice-melting temperatures (T_m) according to the formula by Bodnar (1994).

Electron probe micro analysis (EPMA) was conducted using a JXA-5230F Plus Hyper Probe, with a 10-μm beam diameter, 25-kV accelerating potential, and 10-nA probe current. The following natural mineral or synthetic metal standards were used for the sulfides: Fe (FeS_2), Cu ($CuFeS_2$), Pb (PbS), Zn (ZnS), S (FeS_2), As (GaAs), Sb (Sb_2S_3), Co

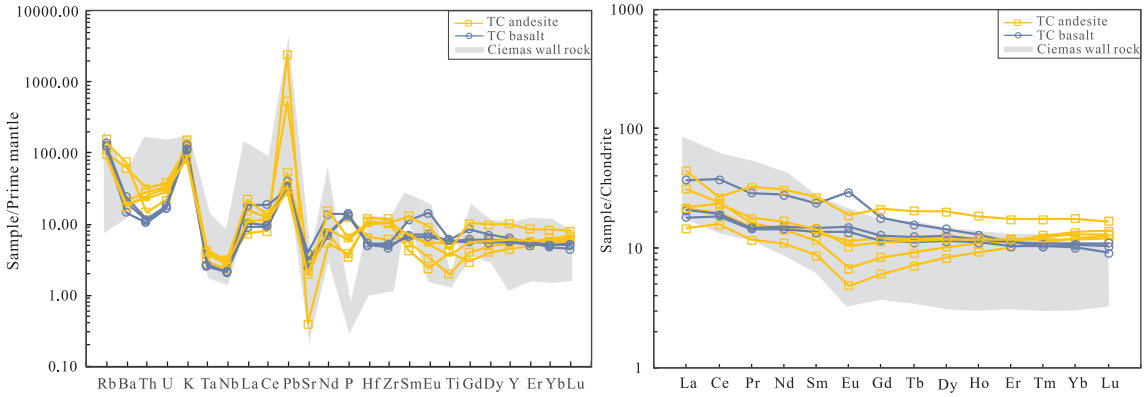

Fig. 8. (a) Spider diagrams of trace elements normalized to the primitive mantle; (b) REE patterns of chondrite samples (Sun and McDonough, 1989). Data for wall rocks in Ciemas (grey region) are from Wu et al. (2015).

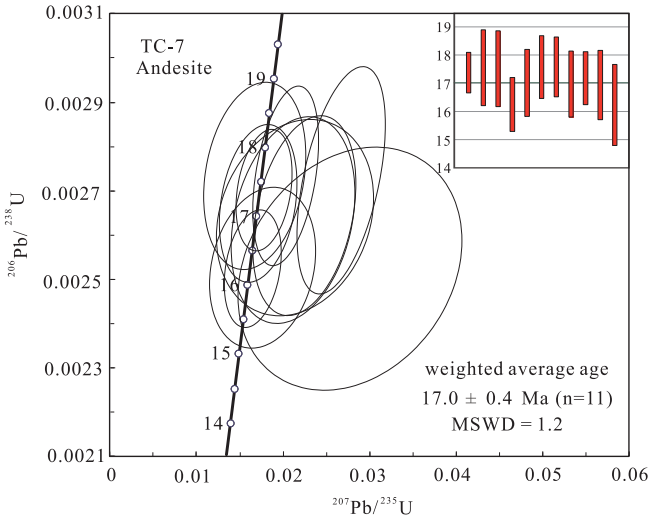

Fig. 9. Zircon U-Pb concordia diagram of andesite in Gunung Subang gold deposit.

(Co), Ni (Ni), Bi (Bi), and Ag (Ag). The data were reduced using the ZAF correction method. The detection limit for Au and Ag were ~360 and 110 ppm, respectively.

5. Analysis results

5.1. Geochemistry of wall rocks

As indicated by petrogeochemistry, the volcanic rocks in Gunung Subang belong to the basalt -andesite group (Fig. 7, Table 3). The volcanic rocks in Gunung Subang have a 48.66–79.17% (average 61.04%) SiO_2 content, with a high content of Al_2O_3 (12.82–20.49%, average 17.61%) and a relatively low content of MgO (0.7–5.7%, average 3.53%). The K content is 2.24–4.18% (average 3.56%). The total alkali content ($Na_2O + K_2O$) is 2.84–3.36%. The results show relatively high LOI (loss on ignition) values that range from 4.76 to 14.77 wt%, with an average of 10.62 wt%. In the Nb/Y-Zr/TiO_2 diagram, half lie in the andesite zone, and a few belong to sub-alkaline basalt.

The trace elements contents of the wall rocks samples are listed in Table 3. The patterns of the primitive mantle-normalized trace elements of the ore samples are markedly different (Fig. 8) in different rock types and the ore has undergone some degree of weathering and leaching,

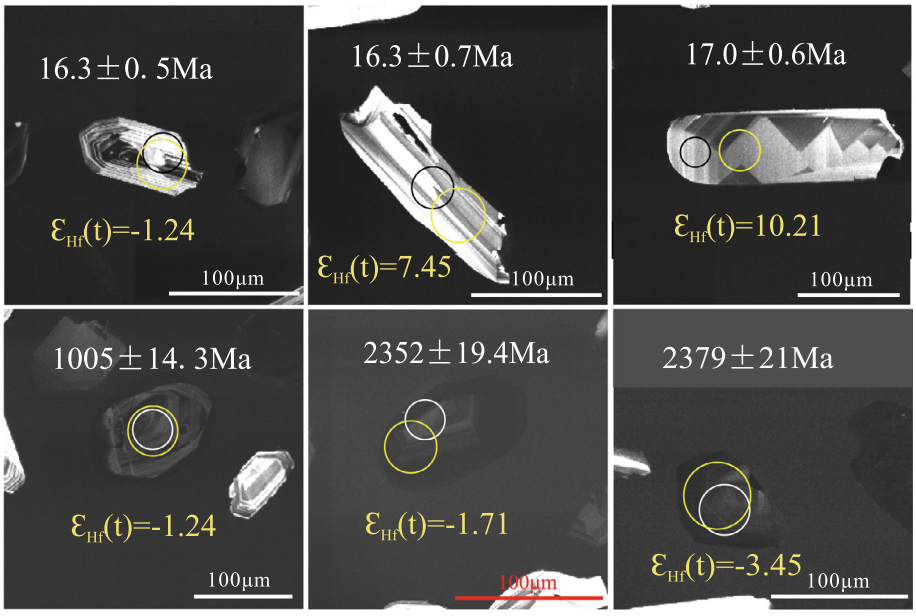

Fig. 10. Cathode luminescence (CL) images of representative zircons analyzed for in-situ U-Pb and Hf isotopes of andesite in the Gunung Subang gold deposit.

Table 4
LA-ICP-MS zircon dating results for magmatic rocks in Gunung Subang.

	^{232}Th	^{238}U	^{207}Pb/^{235}U		^{206}Pb/^{238}U		^{208}Pb/^{232}Th		^{207}Pb/^{206}Pb		^{207}Pb/^{235}U		^{206}Pb/^{238}U		^{208}Pb/^{232}Th	
Analysed point	ppm	ppm	Ratio	1σ	Ratio	1σ	Ratio	1σ	Age (Ma)	1σ	Age (Ma)	1σ	Age (Ma)	1σ	Age (Ma)	1σ
TC-7-4	1783	1140	0.01768	0.00132	0.00270	0.00006	0.00083	0.00003	109	196	17.8	1.0	17.4	0.4	16.8	0.6
TC-7-5	271	352	0.03950	0.00587	0.00273	0.00010	0.0013	0.00008	2125	415	39.3	6.0	17.6	0.7	26.8	1.6
TC-7-6	483	425	0.02663	0.00209	0.00272	0.00010	0.00082	0.00005	1305	255	26.7	2.0	17.5	0.7	16.5	1.0
TC-7-7	2758	1373	0.01635	0.00133	0.00253	0.00005	0.00078	0.00002	122	206	16.5	1.0	16.3	0.4	15.8	0.4
TC-7-8	312	668	0.01747	0.00249	0.00253	0.00007	0.00084	0.00006	553	356	17.6	3.0	16.3	0.5	17.0	1.1
TC-7-9	533	546	0.02229	0.00243	0.00265	0.00009	0.00088	0.00005	628	282	22.4	2.4	17.0	0.6	17.8	1.0
TC-7-10	596	480	0.01660	0.00239	0.00273	0.00009	0.00088	0.00005	256	361	16.7	2.4	17.6	0. 6	17.9	1.0
TC-7-11	504	461	0.02014	0.00156	0.00273	0.00008	0.00094	0.00005	565	278	20.3	1.6	17.6	0.5	18.9	1.0
TC-7-15	647	569	0.02120	0.00371	0.00264	0.00009	0.0009	0.00005	850	332	21.3	3.7	17.0	0.6	18.2	1.0
TC-7-16	1469	772	0.01670	0.00184	0.00267	0.00007	0.00088	0.00003	42.7	280	17.1	1.8	17.2	0.57	17.7	0.6
TC-7-17	398	420	0.02098	0.00293	0.00263	0.00010	0.00077	0.00005	722.0	325	21.1	2.9	17.0	0.6	15.5	0.9
TC-7-20	301	332	0.02757	0.0053	0.00252	0.00010	0.00100	0.00007	2005	506	27.6	5.2	16.3	0.7	20.4	1.4
TC-7-3	84	98	1.70090	0.06660	0.16900	0.00300	0.05200	0.00100	999	75	1009	25.0	1005	14.3	1018	23.4
TC-7-13	251	346	8.76110	0.18800	0.44030	0.00400	0.12000	0.00200	2333	35	2313	19.6	2352	19.4	2379	43.8
TC-7-14	108	241	1.39440	0.04254	0.14760	0.00200	0.04800	0.00100	874	64	887	18.1	888	9.2	951	22.2
TC-7-18	258	572	9.08910	0.18790	0.44640	0.00500	0.30000	0.00200	2305	33	2347	19.0	2379	20.5	2395	42.2
TC-7-19	344	1203	7.90390	0.16970	0.40840	0.00400	0.13000	0.00200	2217	35	2220	19.4	2207	19.6	2464	44.3

Table 5
Hf isotope compositions of Gunung Subang gold deposit.

Samples No.	^{176}Lu/^{177}Hf	1σ	^{176}Yb/^{177}Hf	1σ	^{176}Hf/^{177}Hf	1σ	$\varepsilon_{Hf}(0)$	1σ	εHf(t)	1σ	T_{DM1}	T_{DM2}
TC-7-1	0.000850	0.000006	0.027076	0.000280	0.282211	0.000050	−19.8358	1.840778	1.836805	1.868838	1461.774	1644.707
TC-7-2	0.003323	0.000018	0.127826	0.001200	0.283086	0.000038	11.09728	1.438552	11.43311	1.439202	250.1437	322.0772
TC-7-4	0.003622	0.000047	0.131565	0.002000	0.283108	0.000049	11.8859	1.807296	12.2184	1.808194	218.0988	277.9054
TC-7-5	0.001796	0.000013	0.058429	0.000490	0.282727	0.000029	−1.58785	1.146576	−1.23536	1.14726	759.7387	1031.066
TC-7-6	0.010370	0.000031	0.431561	0.001700	0.282967	0.000036	6.896015	1.372631	7.152574	1.373431	538.0629	562.2865
TC-7-7	0.004702	0.000018	0.192104	0.000980	0.283147	0.000029	13.26864	1.146917	13.58907	1.147651	163.1477	200.7453
TC-7-8	0.006737	0.000043	0.274749	0.002300	0.283139	0.000033	12.96804	1.274973	13.26562	1.275922	187.9457	218.9877
TC-7-9	0.001181	0.000008	0.047480	0.000330	0.281287	0.000022	−52.5264	0.930318	−1.70539	1.04257	2753.403	2909.217
TC-7-10	0.000794	0.000002	0.035926	0.000074	0.282111	0.000029	-23.3863	1.146077	−4.25858	1.177173	1598.613	1885.081
TC-7-11	0.006372	0.000012	0.266693	0.000260	0.283052	0.000027	9.91258	1.084053	10.21413	1.084752	329.608	390.6119
TC-7-12	0.004741	0.000026	0.224306	0.001600	0.283132	0.000029	12.71696	1.146904	13.03692	1.147719	188.0818	231.8431
TC-7-13	0.005800	0.000025	0.236570	0.000830	0.283103	0.000027	11.69493	1.084096	12.00297	1.084924	241.4698	290.049
TC-7-14	0.001137	0.000005	0.041827	0.000170	0.281219	0.000018	−54.9312	0.815638	−3.45129	0.937227	2842.956	3023.823
TC-7-15	0.001292	0.000015	0.051646	0.000690	0.281302	0.000016	−51.9747	0.761825	−4.5308	0.88935	2740.038	2944.75
TC-7-16	0.008363	0.000035	0.330525	0.003200	0.282975	0.000051	7.171856	1.875153	7.450955	1.875912	488.4993	545.6065

Notes: The weighted average ages of zircons are used for calculations of the εHf (t) and the T_{2DM}.
Parameters: $(^{176}Hf/^{177}Hf)^{0}_{CHUR} = 0.282772 \pm 0.000029$, $(^{176}Lu/^{177}Hf)^{0}_{CHUR} = 0.0332 \pm 0.0002$ (Blichert-Toft and Albaréde, 1997); $(^{176}Hf/^{177}Hf)^{0}_{DM} = 0.28325$, $(^{176}Lu/^{177}Hf)^{0}_{DM} = 0.0384$, $f_{DM} = 0.16$ (Griffin et al., 2000), $f_{BBC} = -0.65$ (Rudnick and Gao, 2003). Decay constant: $\lambda = 1.867 \times 10^{-11}\ y^{-1}$(Söderlund et al., 2004); calculation formula: $\varepsilon Hf(t) = [(^{176}Hf/^{177}Hf)^{t}_{spl}/(^{176}Hf/^{177}Hf)^{t}_{CHUR} - 1] \times 10^{4}$, $(^{176}Hf/^{177}Hf)_t = (^{176}Hf/_{177}Hf)_0 - (^{176}Lu/^{177}Hf)_0 (e^{\lambda t} - 1)$, $T_{DM1} = 1/\lambda \ln\{[(^{176}Hf/^{177}Hf)^{0}_{spl} - (^{176}Hf/^{177}Hf)_{0DM}]/[(^{176}Lu/^{177}Hf)^{0}_{spl} - (^{176}Lu/^{177}Hf)^{0}_{DM}] + 1$, $T_{DM2} = T_{DM1} - (T_{DM1} - fspl) \times (f_{BBC} - f_{spl})/(f_{BBC} - f_{DM})$.

Table 6
Sulfur isotope compositions of Gunung Subang gold deposit.

Sample No.	Sample type	Tested mineral	$\delta^{34}S$/‰
TC-14	Au-bearing quartzite	Pyrite	2.97
TC-21	Au-bearing porphyry	Pyrite	1.72
TC-24	Au-bearing quartzite	Pyrite	2.51
TC-26	Au-bearing quartzite	Pyrite	2.37
TC-28	Au-bearing quartzite	Pyrite	2.77
TC-22	Clay breccia	Galena	0.55
TC-26	Au-bearing quartzite	Galena	0.53
TC-15	Argillitization quartzite	Sphalerite	2.44
TC-24	Au-bearing quartzite	Sphalerite	1.58
TC-26	Au-bearing quartzite	Sphalerite	1.98
TC-27	Pb-Zn-bearing quartzite	Sphalerite	1.72

which can be seen by microscope (Fig. 5h). Fig. 8 illustrates the enrichment of the ore samples in Rb, Th, K, Ba (LILE) Zr, and Hf; and the relative depletion of Sr, Nb, Y and Ti (HFSE).

The REE patterns of the volcanic rocks have lightly enriched LREE. TC-4, TC-5, and TC-6 are basaltic with slightly positive Eu anomalies, and δEu 1.09–1.44 (average 1.21); while andesite has δEu 0.67–0.91 (average 0.77) due to the crystallization differentiation of plagioclase. The δCe of TC-7 andesite is 0.7, and that of other andesite and basalt ranges from 1.04 to 1.21 (average 1.12). The REE contents in the volcanic rocks range from 38.1 to 87.35 ppm (average 59.04 ppm). The ratio ΣLREE/ΣHREE ranges from 2.56 to 4.31 (average 2.98). The high LOI (4.76–14.84%, average 10.62) in the volcanic samples suggests that the hydrothermal fluid changed and the source heterogeneity resulted in the geochemical characteristics of the whole rock samples. The depletion in Sr is probably due to alteration, from a poor crystal form of plagioclase (Fig. 5h and i).

5.2. U-Pb dating and Hf isotopes of zircons

The zircons were separated from the andesite in sample TC-7. The zircons are light-colored with length to width ratios of 1:1–4:1. Cathodoluminescence (CL) images of the zircons show clear oscillatory zoning (Fig. 10), typical in magmatic zircons. The Th/U of zircons ranges from 0.29 to 1.56 (average 0.96) in the volcanic rocks. However, some without the oscillatory zoning are dark with core-mantle texture, and these are inherited zircons.

The calculated ^{206}Pb/^{238}U age of the andesite is 17.0 ± 0.4 Ma

Table 7
In situ Pb isotope compositions of Gunung Subang gold deposit.

Samples No.	$^{208}Pb/^{204}Pb$	SE	$^{207}Pb/^{204}Pb$	SE	$^{206}Pb/^{204}Pb$	SE	$^{208}Pb/^{206}Pb$	SE	$^{207}Pb/^{206}Pb$	SE
TC-21-Py1	38.983	0.007	15.669	0.003	18.638	0.003	2.0917	0.0001	0.8408	0.0000
TC-21-Py2	38.819	0.118	15.599	0.047	18.550	0.055	2.0916	0.0005	0.8409	0.0002
TC-21-Py3	39.011	0.012	15.681	0.005	18.649	0.006	2.0917	0.0001	0.8408	0.0000
TC-21-Gn1	38.982	0.005	15.668	0.002	18.639	0.002	2.0912	0.0001	0.8407	0.0000
TC-21-Gn2	38.986	0.006	15.669	0.002	18.642	0.002	2.0911	0.0001	0.8406	0.0000
TC-21-Py4	39.003	0.004	15.675	0.002	18.646	0.002	2.0916	0.0000	0.8407	0.0000
TC-21-Py5	39.009	0.005	15.677	0.002	18.648	0.002	2.0917	0.0001	0.8407	0.0000
TC-21-Py6	39.013	0.006	15.679	0.002	18.647	0.003	2.0919	0.0001	0.8408	0.0000
TC-21-Gn3	38.956	0.007	15.661	0.003	18.629	0.003	2.0911	0.0001	0.8407	0.0000
TC-26-Py1	38.962	0.004	15.663	0.002	18.630	0.002	2.0913	0.0001	0.8407	0.0000
TC-26-Py2	38.934	0.012	15.650	0.005	18.618	0.006	2.0912	0.0001	0.8407	0.0000
TC-26-Gn1	38.974	0.008	15.669	0.003	18.637	0.003	2.0911	0.0001	0.8408	0.0000
TC-26-Gn2	38.956	0.011	15.660	0.004	18.627	0.004	2.0913	0.0001	0.8407	0.0000
TC-26-Gn3	38.979	0.010	15.670	0.004	18.637	0.004	2.0916	0.0001	0.8408	0.0000
TC-26-Gn4	38.969	0.006	15.668	0.002	18.636	0.002	2.0911	0.0001	0.8407	0.0000
TC-26-Py3	38.951	0.021	15.687	0.008	18.653	0.009	2.0881	0.0001	0.8408	0.0001
TC-27-Py5	38.701	0.034	15.606	0.014	18.490	0.016	2.0932	0.0002	0.8440	0.0001
TC-27-Gn1	38.741	0.006	15.631	0.002	18.516	0.002	2.0924	0.0001	0.8442	0.0000
TC-27-Gn2	38.781	0.006	15.636	0.002	18.538	0.002	2.0920	0.0001	0.8434	0.0000
TC-27-Gn3	38.791	0.008	15.641	0.003	18.543	0.003	2.0920	0.0001	0.8434	0.0000
TC-27-Gn4	38.814	0.005	15.643	0.002	18.550	0.002	2.0923	0.0001	0.8433	0.0000
TC-27-Gn5	38.796	0.006	15.634	0.002	18.540	0.002	2.0925	0.0001	0.8433	0.0000
TC1-1-Py1	38.874	0.022	15.663	0.008	18.558	0.009	2.0947	0.0002	0.8441	0.0001
TC1-1-Py2	38.773	0.005	15.628	0.002	18.525	0.002	2.0931	0.0001	0.8437	0.0000
TC1-1-Py3	38.517	0.091	15.557	0.036	18.416	0.043	2.0916	0.0003	0.8449	0.0001
TC1-1-Py4	38.739	0.015	15.641	0.006	18.534	0.006	2.0905	0.0002	0.8440	0.0001

Table 8
Microthermometric result of fluid inclusions for quartz in the Gunung Subang gold deposit.

Sample No.	Size of inclusions (μm)	Gas content (%)	Homogenization temperature (°C)		Final ice-melting temperature (°C)	Salinity (wt% NaCl equiv.)		Type
			Range	Average (quantity)		range	Average (quantity)	
TC-14	5 ~ 19	2 ~ 20	253.4 ~ 363.4	281.7(20)	−3.4 to -0.1	0.2 ~ 5.5	4.4	Quartz-sulfide
TC-23	5 ~ 54	1 ~ 20	253 ~ 363	270.4(22)	−3.9 to −0.1	0.2 ~ 6.2	1.6	Quartz-sulfide
TC-18	4 ~ 65	5 ~ 20	186.2 ~ 269.3	248.2(16)	−3.5 to −0.1	0.2 ~ 5.7	2.9	Quartz Vein
TC-25	15 ~ 39	5 ~ 50	244.3 ~ 260.8	253.7(6)	−0.6 to −0.2	0.4 ~ 1.1	0.7	Euhedral quartz

(MSWD = 1.2, n = 11) (Fig. 9). This is within the acceptable range of experimental error, implying that the andesite formed during the Mid-Miocene. Several inherited zircons were also found (Table 4), from 999 ± 75 Ma, 2333 ± 35 Ma, 874 ± 64 Ma, 2305 ± 33 Ma, and 2217 ± 35 Ma.

Sixteen zircons were chosen to conduct the Hf isotope analysis. In magmatic zircons the ε_{Hf} (t) of the andesite is relatively consistent at −1.23–17.19, and at −4.53 to 1.84 in inherited zircons (Fig. 10, Table 7). The calculated two stage model ages (T_{DM2}) of the magmatic zircons are 200–3023 Ma Table 9.

5.3. Sulfur and in-situ Pb isotopes of sulfides

The sulfur compositions of galena, sphalerite and pyrite are 0.55–0.53‰, 1.58–2.44‰ and 1.72–2.97‰, respectively. The results of the in-situ Pb isotopic composition of sulfide in Gunung Subang are given in Table 6. The average ratios of $^{206}Pb/^{204}Pb$, $^{207}Pb/^{204}Pb$, and $^{208}Pb/^{204}Pb$ from pyrite are 18.586 ± 0.012, 15.648 ± 0.01 and 38.878 ± 0.026, respectively. In galena, the Pb content ratios are 18.594 ± 0.003, 15.654 ± 0.003, 38.894 ± 0.007, respectively.

5.4. Fluid inclusions petrographic and microthermometry

Sixty-four fluid inclusions of four samples taken from Celak were examined in total (Fig. 11), and can be classified into three types according to the host mineral: quartz-sulfide vein, quartz vein, and euhedral quartz. Most of them are < 15 μm. Individual inclusions are irregular or regular. The regular inclusions exhibit negative crystal, oval, or triangular shapes, and are aqueous, consisting of both two phases (liquid and vapor) and single-phase at room temperature. The former is common, liquid-rich, and relatively large; while the latter are rare and small. The inclusions in strongly silicified samples are scarce and relatively small in size. Combining these observations with the results of the Raman spectroscopy it was found that some fluid inclusions contain only a small amount of N_2, and neither double-edged CO_2 or daughter minerals were observed. The gas percentage of the two-phase inclusions ranges from 5% to 20%. The fluid inclusions are distributed both in isolation and in clusters within individual crystals, indicating that the inclusions are both native and secondary inclusions.

Based on the measurement of fluid inclusions in the ore in the Celak block, the hydrothermal fluid in the Gunung Subang area has a homogenization temperature (Th) of between 186.2 °C and 363.4 °C; a melting temperature (T_m) between −4.3 °C and −0.2 °C; and salinity between 0.18 and 6.80 wt% NaCl. The results of each vein are shown in Table 8.

In the quartz-sulfide vein, a total of forty-one homogenization temperatures (T_h) of the inclusions were measured. The determined values range from 253.4363.4 °C (with a gap between 320 and 350 °C), with an average of 281.7 °C. Below 360 °C, the Th data have peaks at 260–280 °C. Homogenization temperatures for sixteen of the fluid inclusions were measured from the quartz vein, with values in the range of 186.2–269.3 °C and an average of 248.2 °C, and values concentrated

Table 9
EPMA results for pyrite in Gunung Subang.

No.	Stage	Se	As	Fe	S	Cu	Zn	Sb	Ni	Co	Au	Ag	Te	Total
TC-21-Py1	I	< mdl	< mdl	46.69	53.99	< mdl	< mdl	< mdl	< mdl	0.042	< mdl	< mdl	< mdl	100.75
TC21-Py6	I	< mdl	1.00	46.30	52.97	< mdl	0.02	< mdl	< mdl	0.049	0.04	0.03	< mdl	100.42
TC-26-1 Py	I	< mdl	< mdl	4.09	32.35	3.45	59.67	< mdl	0.02	0.017	< mdl	< mdl	< mdl	99.61
TC-26-3Py	I	< mdl	0.48	46.26	53.26	< mdl	0.28	< mdl	< mdl	0.025	< mdl	< mdl	< mdl	100.32
TC-26-Py4	I	< mdl	0.46	46.02	53.17	0.02	0.92	< mdl	< mdl	0.033	0.05	< mdl	0.031	100.70
TC-26-Py5	I	< mdl	0.12	46.22	53.13	0.02	0.17	< mdl	< mdl	0.046	0.03	< mdl	< mdl	99.76
TC-26-Py7	I	< mdl	< mdl	45.99	53.40	0.03	0.35	0.02	< mdl	0.032	< mdl	< mdl	< mdl	99.82
TC-26-Py13	I	< mdl	< mdl	46.76	53.84	< mdl	0.02	< mdl	< mdl	0.047	< mdl	< mdl	< mdl	100.66
TC-27-Py4	I	< mdl	< mdl	46.60	54.06	< mdl	< mdl	< mdl	< mdl	0.042	0.04	< mdl	< mdl	100.75
TC-27-Py5	I	< mdl	< mdl	46.72	54.29	< mdl	< mdl	< mdl	< mdl	0.035	0.04	< mdl	0.095	101.20
TC-27-Py8	I	< mdl	0.04	46.47	53.42	< mdl	< mdl	< mdl	0.029	0.056	< mdl	< mdl	< mdl	100.09
TC-21-Py2	II	< mdl	1.76	45.97	52.11	0.02	< mdl	0.03	0.019	0.042	< mdl	0.02	< mdl	99.98
TC21-Py5	II	< mdl	0.56	46.54	53.11	< mdl	< mdl	0.02	< mdl	0.037	0.08	< mdl	< mdl	100.35
TC21-Py7	II	< mdl	0.09	46.11	53.20	< mdl	< mdl	< mdl	< mdl	0.028	0.06	< mdl	< mdl	99.50
TC21-Py8	II	< mdl	0.08	46.58	53.39	< mdl	< mdl	< mdl	< mdl	0.027	< mdl	0.01	< mdl	100.10
TC-21-Py9	II	< mdl	0.15	46.40	53.45	0.02	< mdl	< mdl	< mdl	0.042	< mdl	< mdl	< mdl	100.10
TC-26-2Py	II	< mdl	0.37	46.37	53.18	< mdl	0.87	0.02	< mdl	0.031	< mdl	< mdl	0.031	100.90
TC-26-Py6	II	< mdl	1.19	44.59	52.50	0.10	0.24	< mdl	< mdl	0.035	0.03	0.03	0.084	98.82
TC-26-Py8	II	< mdl	0.12	46.11	52.96	< mdl	0.04	< mdl	< mdl	0.032	0.05	0.02	< mdl	99.32
TC-26-Py9	II	< mdl	0.11	46.48	53.50	< mdl	< mdl	< mdl	< mdl	0.049	0.10	< mdl	< mdl	100.24
TC-26-Py10	II	< mdl	0.12	45.37	53.10	< mdl	0.02	< mdl	< mdl	0.031	0.05	< mdl	< mdl	98.69
TC-26-Py11	II	< mdl	0.03	46.49	52.73	0.15	0.11	< mdl	< mdl	0.026	0.07	< mdl	< mdl	99.63
TC-26-Py12	II	< mdl	0.81	46.08	52.70	0.03	0.04	0.04	< mdl	0.037	< mdl	< mdl	0.039	99.77
TC-26-Py14	II	< mdl	0.34	45.87	52.78	< mdl	< mdl	0.02	< mdl	0.041	< mdl	< mdl	0.031	99.11
TC-26-Py15	II	< mdl	< mdl	45.79	52.09	0.02	< mdl	< mdl	< mdl	0.045	0.04	< mdl	0.056	98.06
TC-26-Py16	II	0.062	< mdl	46.70	53.84	< mdl	0.12	< mdl	< mdl	0.045	< mdl	< mdl	0.056	100.79
TC-26-Py17	II	< mdl	0.30	46.40	53.40	< mdl	0.04	< mdl	< mdl	0.043	< mdl	< mdl	< mdl	100.20
TC-26-Py14	II	< mdl	0.55	45.70	52.11	< mdl	0.02	0.02	< mdl	0.029	0.04	< mdl	0.036	98.51
TC-26-Py15	II	< mdl	< mdl	46.61	53.60	< mdl	< mdl	< mdl	< mdl	0.034	0.03	< mdl	< mdl	100.28
TC-26-Py17	II	< mdl	0.30	46.40	52.48	0.02	< mdl	< mdl	< mdl	0.039	0.05	0.04	< mdl	98.78
TC-26-Py18	II	< mdl	0.29	46.40	53.21	< mdl	0.02	< mdl	< mdl	0.03	< mdl	< mdl	< mdl	99.97
TC-26-Py19	II	< mdl	0.24	46.56	53.05	< mdl	0.02	< mdl	< mdl	0.038	< mdl	< mdl	0.048	99.95
TC-27-Py1	II	< mdl	< mdl	46.69	53.53	< mdl	< mdl	< mdl	< mdl	0.057	0.08	< mdl	< mdl	100.35
TC-27-Py2	II	< mdl	1.76	45.97	53.26	< mdl	< mdl	< mdl	< mdl	0.035	< mdl	< mdl	< mdl	99.75
TC-27-Py3	II	0.052	< mdl	46.24	53.42	0.03	0.03	< mdl	< mdl	0.034	0.04	0.01	< mdl	99.86
TC-27-Py6	II	0.084	< mdl	46.42	54.29	< mdl	< mdl	< mdl	< mdl	0.031	< mdl	< mdl	< mdl	100.84
TC-27-Py7	II	0.067	0.05	46.87	53.69	< mdl	< mdl	< mdl	< mdl	0.047	0.03	< mdl	< mdl	100.76
TC-21-Sph1	II	na	< mdl	1.20	33.52	0.99	65.37	0.03	na	na	< mdl	< mdl	na	101.11
TC-21-Sph3	II	na	0.15	1.15	32.79	0.78	65.06	< mdl	na	na	0.05	< mdl	na	99.98
TC-21-Sph4	II	na	< mdl	1.28	33.27	0.88	65.13	< mdl	na	na	< mdl	< mdl	na	100.63
TC-26-Sph1	II	na	< mdl	1.41	32.69	< mdl	65.41	< mdl	na	na	< mdl	< mdl	na	99.52
TC-26-Sph2	II	na	< mdl	1.92	32.95	1.62	63.88	< mdl	na	na	< mdl	< mdl	na	100.47
TC-26-Sph3	II	na	< mdl	3.95	33.41	4.14	59.27	< mdl	na	na	0.09	< mdl	na	100.91
TC-27-Sph1	II	na	< mdl	1.88	32.86	< mdl	64.41	< mdl	na	na	< mdl	< mdl	na	99.26
TC-27-Sph2	II	na	0.04	1.36	33.06	< mdl	65.61	< mdl	na	na	0.07	< mdl	na	100.27
TC-27-Sph3	II	na	< mdl	1.21	33.31	0.12	65.82	< mdl	na	na	< mdl	< mdl	na	100.49
TC-27-Sph4	II	na	< mdl	1.09	33.42	0.34	65.30	< mdl	na	na	< mdl	< mdl	na	100.21
TC-27-Sph5	II	na	0.05	1.58	33.20	0.17	65.06	< mdl	na	na	< mdl	< mdl	na	100.12
TC-I-1-Sph1	II	na	< mdl	1.67	33.13	1.17	64.43	< mdl	na	na	< mdl	< mdl	na	100.47
TC-I-1-Sph2	II	na	< mdl	1.24	33.85	0.22	65.76	< mdl	na	na	< mdl	< mdl	na	101.14
TC-I-1-Sph3	II	na	0.05	1.68	32.23	1.22	64.15	< mdl	na	na	< mdl	< mdl	na	99.43
TC-I-1-Ccp1	II	na	< mdl	31.03	35.74	35.04	0.04	< mdl	na	na	< mdl	< mdl	na	101.86
TC-I-1-Ccp2	II	na	< mdl	30.93	36.01	34.71	0.05	< mdl	na	na	< mdl	< mdl	na	101.74
TC-I-1-Ccp3	II	na	0.05	30.95	35.75	34.74	< mdl	< mdl	na	na	0.07	0.02	na	101.67
TC-I-1-Ccp4	II	na	< mdl	31.02	35.60	34.79	< mdl	< mdl	na	na	< mdl	< mdl	na	101.44
TC-I-1-Ccp5	II	na	< mdl	28.07	35.90	34.86	0.02	< mdl	na	na	0.04	0.01	na	98.94
TC-26-Gn1	II	na	< mdl	0.03	13.51	< mdl	< mdl	< mdl	na	na	< mdl	< mdl	na	100.12
TC-26-Gn2	II	na	< mdl	0.05	13.17	0.02	< mdl	< mdl	na	na	< mdl	< mdl	na	98.09
TC-27-Gn2	II	na	< mdl	2.05	33.72	< mdl	65.09	< mdl	na	na	0.06	< mdl	na	100.95
TC-27-Gn4	II	na	< mdl	0.14	13.48	< mdl	< mdl	< mdl	na	na	< mdl	< mdl	na	99.83
TC-I-1-Py6	III	< mdl	0.20	46.56	53.34	< mdl	< mdl	< mdl	< mdl	0.037	0.06	< mdl	< mdl	100.21
TC-I-1-Py7	III	< mdl	< mdl	46.86	53.83	0.02	0.03	< mdl	< mdl	0.057	0.05	< mdl	< mdl	100.88
TC-I-1-Py8	III	< mdl	< mdl	46.76	53.88	< mdl	< mdl	< mdl	< mdl	0.047	< mdl	< mdl	0.048	100.98
TC-I-1-Py9	III	< mdl	< mdl	46.68	53.71	0.05	< mdl	< mdl	< mdl	0.055	0.08	< mdl	< mdl	100.62
TC-I-1-Py10	III	< mdl	0.07	46.77	53.61	0.05	< mdl	< mdl	< mdl	0.044	0.05	< mdl	0.028	100.62
TC-I-1-Py11	III	< mdl	< mdl	46.76	53.51	< mdl	< mdl	< mdl	< mdl	0.031	0.03	0.03	0.056	100.43

Notes: Na = not analyzed; mdl = minimum detection limit.
TC -sample from the Celak ore block.

at 260–270 °C. The homogenization temperatures of six inclusions were measured from the euhedral quartz, with values of 244.3–260.8 °C, an average of 253.7 °C, and four values occurring in the range of 250.4–258.8 °C.

In ore from the quartz-sulfide vein, the final ice-melting temperatures ($T_{m\text{-}ice}$) of FIs lie between −3.9 and −0.1 °C, with corresponding salinities ranging from 0.2 to 6.2 wt% NaCl. In the quartz vein, the $T_{m\text{-}ice}$ of FIs are between −3.5 and −0.1 °C, with corresponding salinities

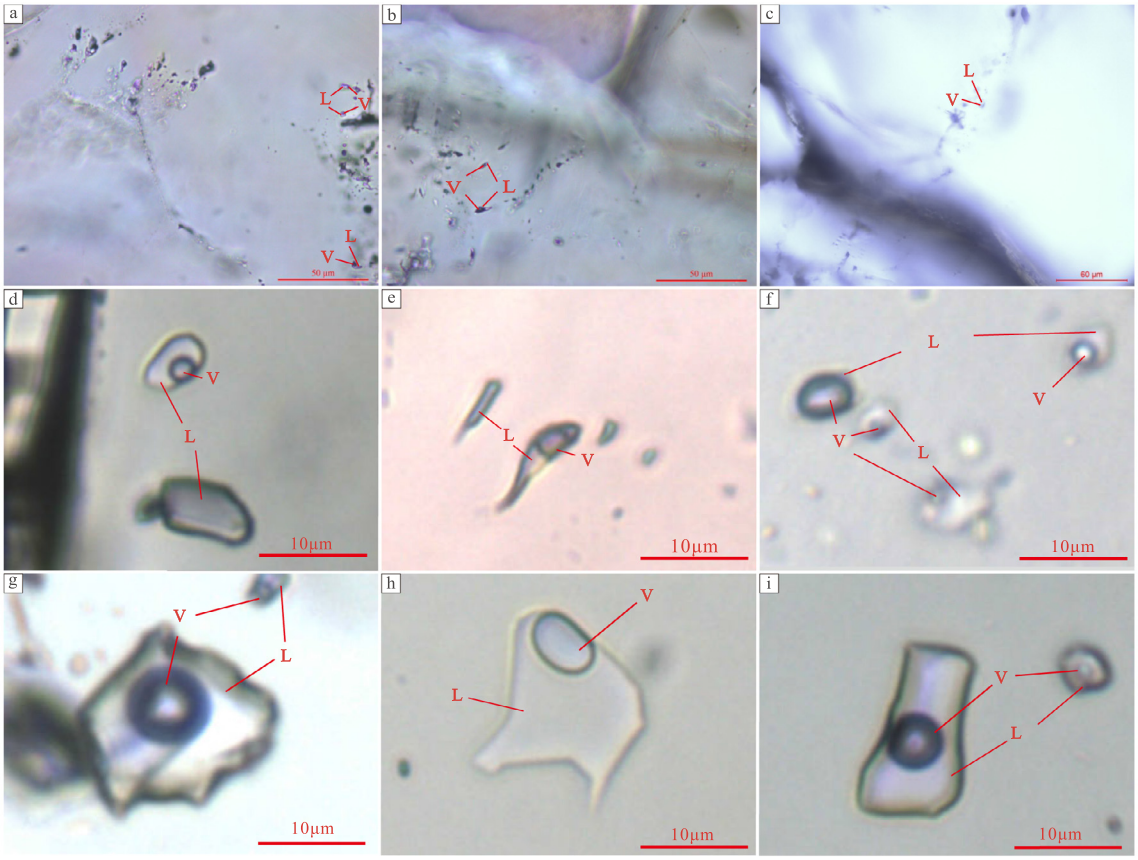

Fig. 11. Micrographs of fluid inclusions. (a) A cluster of inclusions (primary or pseudosecondary), from TC-23; (b) Linearly distributed inclusions, from TC-23. (c) Small regular fluid inclusions in clean quartz crystal. (d) A liquid-rich two phases inclusion from TC-23. (e) Linearly distributed inclusions in clean quartz crystal, from TC-23. (f) A liquid-rich two phases inclusion, from TC-14. (g) An ovate fluid inclusion, from TC-18. (h) A negative crystal inclusion with high gas content, from TC-23. (i) A near- shape fluid inclusion, from TC-25. L represent liquid, V represents vapor.

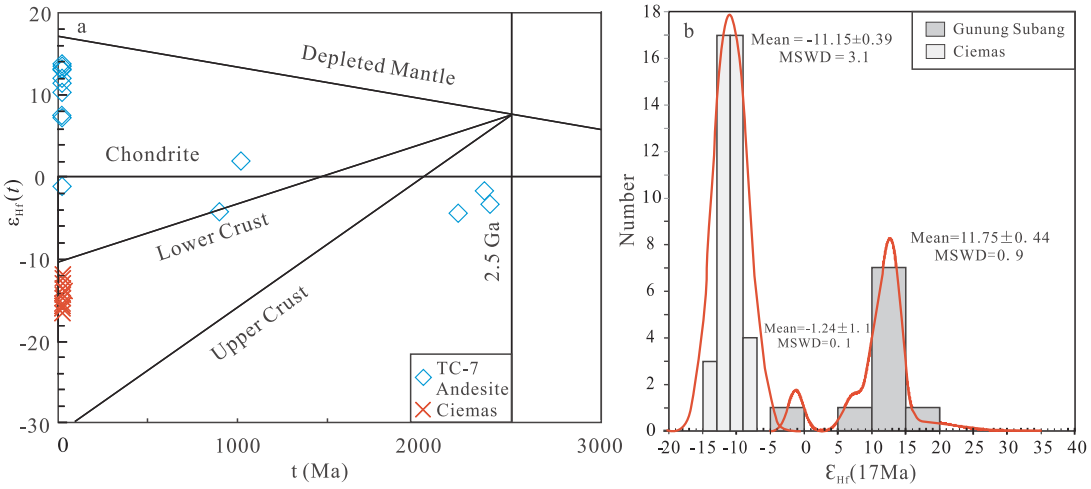

Fig. 12. (a) Zircon $\varepsilon_{Hf}(t)$ values versus age of andesite in the Gunung Subang and Ciemas gold deposits; (b) Histograms of zircon $\varepsilon_{Hf}(t)$ values, after Wu et al. (2019).

of 0.2–5.7 wt% NaCl. In euhedral quartz, the $T_{m\text{-}ice}$ of FIs are between −0.6 and −0.2 °C, with corresponding salinities of 0.4–1.1 wt% NaCl. As a whole, the values are concentrated in the range from 0.2 to 6.2 wt % NaCl.

5.5. Mineralogy of Gold-bearing minerals

Four samples taken from Celak were selected for electron microprobe analysis. Sample 21 is a hydrothermal breccia type ore. Sample 26 is a quartz vein type ore. Samples 26 and 27 are of quartz vein type ore. Sample I-1 is a gold-bearing pyrite disseminated ore. According to the microscopic observation of the Gunung Subang gold ore, Au is mainly found in PyII and PyIII, at 300–400 ppm and 300–600 ppm, respectively. In addition, the framboidal pyrite also contains ~300 to 400 ppm Au.

According to SEM and EPMA results, gold mainly occurs as telluride in the Gunung Subang gold deposit, including krennerite, hessite, and kurilite. They are mainly hosted in the pyrite, and increase in content

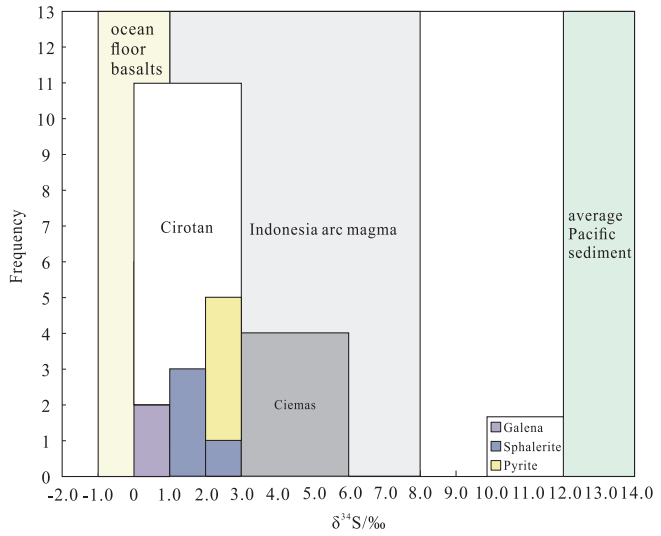

Fig. 13. Sulfide compositions in the Gunung Subang gold deposit (Data sources: Hoog et al., 2001; Alt and Burdett, 1992; Sakai et al., 1984).

from the early to late period, meaning that pyrite is major Au-bearing mineral. The gold content is 0.03–0.98 wt% (average 0.1 wt%) in pyrite, 0.05–0.07 wt% (average 0.07 wt%) in sphalerite, 0.04–0.07 wt% (average 0.055 wt%) in chalcopyrite, and 0.06 wt% (average 0.06 wt%) in galena. There also may be minor amounts of native gold in pyrite.

6. Discussion

6.1. Magmatism associated with mineralization

Java is the east part of the Sunda Arc, which contains a series of magmatic rocks since the Eocene (Van, 1970; Katili, 1975; Nicholls et al., 1980). Based on the K-Ar dating results, Soreia et al. (1994) proposed that volcanisms in Java can be divided in to three magmatic events: the Late Eocene to early Miocene (40–19 or 18 Ma), the late Miocene to Pliocene (12 or 11–2 Ma), and the Quaternary. The Late Miocene to early Miocene belt was emplaced along the southern part of Java, trending from west to east. The late Miocene to Pliocene belt occurs further north, is parallel to the older belt, and is in places overlain by Quaternary volcanics.

The Gunung Subang gold deposit is located in an active volcanic zone in southern Java, and the mining area exposed quartz andesite and tuff breccia. The zircon U-Pb ages represent the eruptive magma crystallization periods (Table 4), and their ages are very close to each other within the error ranges (Fig. 10), demonstrating that they belong to late Eocene to Mid-Miocene igneous activities. In previous research, epithermal and porphyry deposits formed in 1.7–11.2 Ma gained more focused in West Java, except for Ciemas, which was proved to formed in 16.9–17.5 Ma (Wu et al., 2014). The LA-ICP-MS U-Pb zircons ages of the andesite in Gunung Subang is 17.0 ± 0.4 Ma (MSWD = 1.2, n = 11) (Fig. 9), which is close to that of Ciemas, suggesting the magmatism associated with mineralization occurred in the Mid-Miocene.

Based on microscopic observation and the relatively high LOI (4.76–14.77%) of the volcanic rock, it is indicated that the rocks are weakly altered (Table 3). The plot in a Zr/TiO_2 vs. Nb/Y diagram is often used to distinguish volcanic rocks with hydrothermal alteration, and the diagram indicates basalt-andesite compositions, which are common in the volcanic belts of island-arcs. The K content (average 3.56%) is higher than that of volcanic rocks in southern Java and other arc settings (average 1.6%), but it is close in value to active continental margin (average 3.25%) (Li and Li, 2016). This may be attributed to the older age of the volcanic rock, as the composition of younger magmas belongs to the high-K or tephrite series. In general, the volcanic rocks are rich in K and Al, but depleted in alkaline and Ti, which is characteristic of volcanic arc settings.

The enrichment in the large-ion lithophile elements (LILEs) K, Rb, Th and U, and depletion in the high-field strength elements (HFSEs) Nb, Ta, and P are the major geochemical characteristics of arc magmatic rocks (Kay, 1980; Perfit et al., 1980). The fluid from the dehydration of subducted slab results in a partial melting of the overlying mantle wedge (Morris et al., 1990; Sigmarsson et al., 1990). Comparing the composition of sediments in the subduction zone to those of the magma indicates that the enrichment of LILE arc magmatic rocks stems from the addition of sediments from the oceanic crust (Plank and Langmuir, 1993). However, the Pb in Gunung Subang volcanic rocks are lower than that in Ciemas (Fig. 8a), indicating a lower degree of contamination in the crust. The special geochemical features reflect the specialization of the magma resources or partial melting processes. The $(La/Yb)_N$ ratios of volcanic rocks are 1.27–3.88 (average 2.21), indicating low REE fractionation, similar to that of typical calc-alkaline lavas (Martin, 1999). High Y contents (average 25.65 ppm) and high Yb contents (average 2.61 ppm) clearly distinguish these from adakites, which originate from the partial melting of oceanic crust (Defant and Drummond, 1990; Martin, 1999). It is therefore produced by the partial melting of the mantle wedge.

The geochemical characteristics of the volcanic rocks indicates that they originated from the arc magmatism event. As the Indian-Australian Plate was subducted beneath the Eurasian Plate, the addition of fluid from the dehydration of the overlying mantle wedge generated mafic magma. This evolved further in the crust, resulting in the Mid-Miocene arc magmatism in the Gunung Subang area.

Some inherited zircons were also found (Table 4), from 999 ± 75 Ma, 2333 ± 35 Ma, 874 ± 64 Ma, 2305 ± 33 Ma, and 2217 ± 35 Ma. These older zircons usually show strong involvement of an old crustal component (Fig. 12). Thus, they may come from ancient

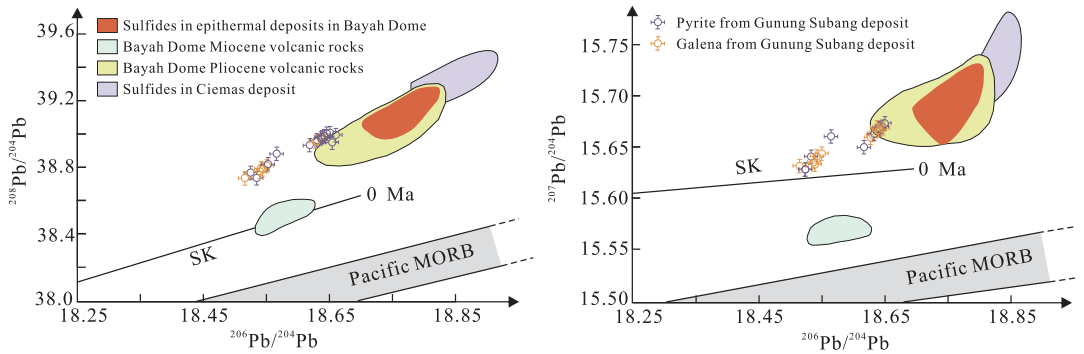

Fig. 14. Lead-isotope diagrams of sulfides in the Gunung Subang gold deposit, West Java. SK: evolution curve from Stacey (1975); Pb isotope data of Miocene and Pliocene volcanic rocks and sulfides of epithermal deposits in Bayah Dome from Marcoux (1994).

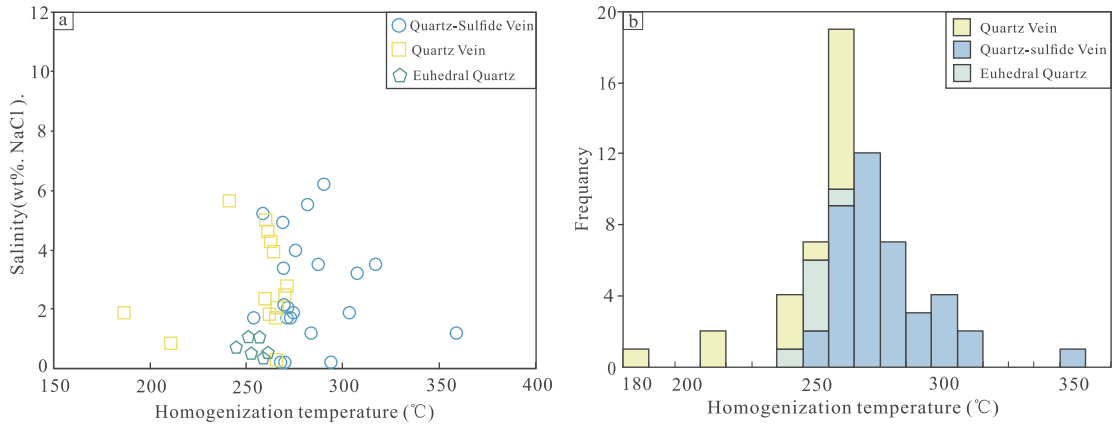

Fig. 15. (a) Th versus salinity diagram in the Gunung Subang deposit. (b) Histogram of valid homogenization temperatures for different types of fluid inclusion.

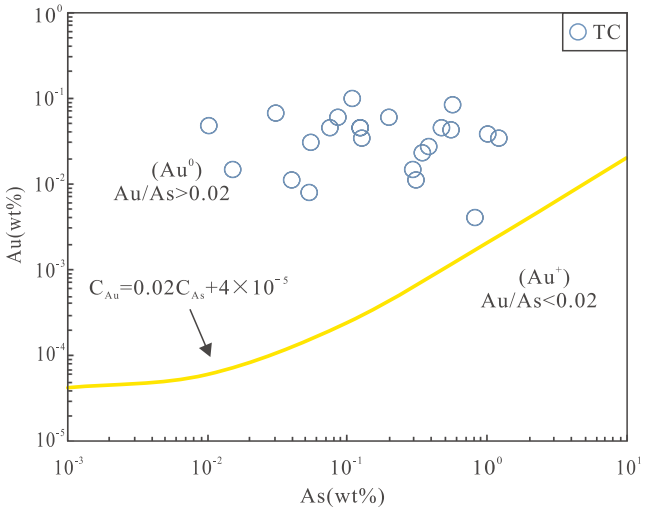

Fig. 16. Relationship between Au and As in pyrite (based on Reich et al., 2005).

Sundaland, indicating that the magma was contaminated with ancient crust during upwelling.

As is shown in Fig. 12 and Table 5, the zircons $\varepsilon_{Hf}(t)$ of the Gunung Subang are not consistent. The Hf isotope compositions of magmatic zircons are mainly positive, with a mean $\varepsilon_{Hf}(t)$ value of 9.91 ± 1.64, indicating that the arc magmatism underwent the contamination with juvenile crust. However, some inherited zircons were discovered in the volcanic rock, suggesting that the magmatism was contaminated with the ancient crust. This observation, combined with the coeval magmatism in the Ciemas, located in the west, whose arc magmatism was strongly contaminated with Sundaland (ε_{Hf} (t) = −11.5 ± 0.39), it can be concluded that the degree of contamination with ancient crust in coeval (~17 Ma) arc magmatism decreased from the east to west in West Java. The calculated two stage model age (T_{DM2}) of the andesite magmatic and inherited zircons is 200–3023 Ma. The T_{DM2} of all zircons is older than the U-Pb ages, implying that it was not directly formed by fractional crystallization of mantle-derived material, but by partial melting of igneous crustal material. Thus, we suggest that Mid-Miocene arc magmatism in Gunung Subang predominantly contaminated with juvenile crust, and slightly contaminated with Sundaland.

6.2. Ore-forming material source

Gold-silver-telluride is a newly discovered mineral in the Gunung Subang deposit. Te is an element that shows affinity to the mantle-core, with low water solubility and a tendency towards concentration in sulfides (Afifi et al., 1988). Many deposits can be associated with Te, the genesis of which shows an affinity with deep magmatism and mantle, such as the Dongping Au-Te deposit (Mao and Li, 2001) and the Yinggezhuang gold deposit (Zhou et al., 2011) in China. The occurrence of Te reflects the contribution of mantle to a degree, although there is not a large amount of telluride in the Gunung Subang deposit. This indicates that there was some Te in the ore-forming fluid and that there was a high geochemical background value for Te in the origin of ore formation. The origin of the ore-forming materials shows affinity with the mantle.

The sulfur compositions in Gunung Subang are very uniform, ranging from 0 to 3‰ (Fig. 13), suggesting that the sulfur sources may be the same and are of the deep magmatic sulfur. Compared with the sulfur isotope composition of Cirotan (Wagner et al., 2005) and Ciemas (Zhang et al., 2015; Zheng et al., 2015), with a mean of 3.8 ± 0.9 and 5.54 ± 0.06‰, respectively. The sulfur isotope composition of the Gunung Subang gold deposit is more like that of Cirotan, a younger (1.7 Ma) low-sulfidation epithermal deposit in Bayah Dome. The $\delta^{34}S$ values of ore samples are lower than those of West Java Guntur lava flows (average 4.7 ± 1.4‰), which are considered to have a magma source mixed with continental basement sediments (Hoog et al., 2001). Thus, the ore-forming materials source of the Gunung Subang may mainly be magmatic.

The Pb isotopes of the sulfides (galena and pyrite) are partly consistent with radiogenic Pb (Fig. 14). The mean ratios of $^{206}Pb/^{204}Pb$, $^{207}Pb/^{204}Pb$ and $^{208}Pb/^{204}Pb$ are 18.59 ± 0.007, 15.65 ± 0.007 and 38.89 ± 0.017, respectively. These ratios are partly similar to the Pb isotopes of Pliocene volcanic rocks. According to Marcoux and Milési (1994), the lead-isotopic compositions of Miocene volcanic rocks show mantle affinity, whereas the lead of Pliocene volcanic rocks and Miocene-Pliocene gold deposits is highly radiogenic and clearly of crustal source in an underlying Precambrian crust. The lead-isotopic compositions of the Gunung Subang deposit lie between these extremes, indicating that ore-forming materials mainly come from Miocene to Pliocene volcanic rocks, and some mantle-derived materials may also be added.

6.3. Evolution of ore-forming fluid and occurrence of Au

Fluid inclusions study indicates that temperature and salinity of ore-forming fluid in epithermal deposits are lower than that of porphyry deposits, but stable isotope characteristics suggest that they both come from magma system (Heinrich, 2007). Many geochemists have researched on the ore-forming fluid evolution characteristics of porphyry and epithermal system (Hedenquist et al., 1998; Hinrich, 2005; Heinrich et al., 2004; Richards, 2009). In the Gunung Subang, there are mainly two phases (liquid and vapor) and single-phase at room temperature, with no mineral or CO_2 observed, in accordance with Heinrich's research into fluid inclusions of epithermal deposits (Heinrich,

Table 10
Summary of mineralogic, age and geochemical characteristics of the Se- and Te-types of West Java ore deposits (modified after Yuningsih et al., 2014).

Deposit	Se- and Te-minerals	Sulfosalt	Sulfide and other minerals	Host rocks	Gangue, and alteration-mineralization	Mineralization age (Ma)	Th/°C	Salinity/wt% NaCl
Se-Type								
Pongkor (Basuki et al., 1994; Marcoux and Milési, 1994; Milési et al., 1999)	Aguilarite, trace hessite	Tetrahedrite, famatinite, proustite, pearceite-polybasite, antimony	Pyrite, chalcopyrite, sphalerite, galena, uytenbogaardtite, chalcocite, stromeyerite, mckinstryite, acanthite, bornite, electrum, Au-Ag alloy, willemite, massicot, manganese oxide, limonite	Andesitic breccia, tuff, lapilli, andesite intercalated limestone and sandstone (Oligocene-Early Miocene	Quartz, calcite, dolmite kutnohorite, carbonate, rhodochrosite, adularia, montmorilonite, illite/smectite, kaolinite, K-feldspar	2.05–2.7	Carbonate: 171–249; quartz:180–287; sphalerite: 220–320	Carbonate: 0.5 ± 0.6; quartz: 0–0.5
Cikidang (Rosana and Matsueda, 2002)	Aguilarite		Pyrite, sphalerite, galena, electrum, manganese oxide, limonite	Volcanic rock of lapilli tuff and breccia (Early Miocene)	Smectite/chlorite mixed layer mineral, epidote, carbonate, illite, quartz, kaolinite, limonite, montmorilonite, adularia	2.4	Quartz: 170–260	Quartz: < 3.0
Cibaliung (Angeles et al., 2002; Harijoko et al., 2004)	Aguilarite-naumannite, trace altaite, hessite	Tennantite-tetrahedrite, polybasite	Pyrite, sphalerite, galena, arsenopyrite, marcasite, argentite-stromeyerite, trace chalcopyrite, bornite, electrum, rare native silver	Basaltic andesite volcanics intercalated tuffaceous sediment (Middle-Late Miocene)	Quartz, adularia, calcite, smectite, illite, mixed layered chlorite-smectite and illite-smectite, kaolinite, epidote, zeolite	11.18–10.65	Quartz: 160–330 (170-shallow), 170–300 (220-deep)	Quartz: < 1.0
Cirotan (Milési et al., 1994; Marcoux et al., 1993)	Aguilarite	Tetrahedrite, polybasite, pyrargyrite	Pyrite, marcasite, galena, chalcopyrite, pyrrhotite, sphalerite, arsenopyrite, acanthite, mackinawite, uytenbogaardtite, covellite, electrum, scheelite, cassiterite, canfieldite, lillianite, wolframite	Calc-alkaline rhyolitic-dacitic, quartz microdiorite (Miocene) cutting volcano-sedimentary series	Chlorite, epidote, quartz, calcite, rare Fe-Ti oxides, illite/smectite, kaolinite, adularia, apatite, rare gypsum, anhydrite	1.7	Quartz: 180–255; sphalerite: 207–280	Sphalerite: 2.89–7.15
Te-type								
Arinem (Yuningsih et al., 2012)	Hessite, altaite, tetradymite, stutzite, petzite	Enargite, tennantite, tetrahedrite	Sphalerite, galena, chalcopyrite, pyrite, marcasite, arsenopyrite, pyrrhotite, argentite, covellite, chalcocite, electrum, hematite	Andesitic tuff, tuff breccias, lava (Oligocene-Middle Miocene)	Quartz, calcite, sericite, illite, mixed layered illite-chlorite, chlorite-smectite, kaolinite	8.8–9.9	Quartz: 157–327; sphalerite: 153-275; calcite: 140-217	Quartz: 0.2–4.3; sphalerite: 0.9–3.9; calcite: 1.2–3.9
Cineam (Widi and Matsueda, 1998)	Hessite, petzite, aguilarite	Tetrahedrite-tennantite, pyrargyrite, proustite	Pyrite, sphalerite, galena, arsenopyrite, chalcopyrite, argentite, realgar, stibnite, orpiment, electrum, iron-oxide	Andesitic-dacitic volcanic rocks (Oligocene-Miocene) intruded by diorite, granodiorite, andesite and dacite intrusive	Quartz, illite, calcite, propylite, argillic, silicification and locally phyrophylite	8.5–9.6	Quartz: 190–240, up to 350	Quartz: 1.45–2.3, up to 3.7
Gunung Subang	Hessite, Krennerite, petzite	Tetrahedrite	Pyrite, sphalerite, galena, chalcopyrite, iron-oxide	Breccia, tuff and andesite (Tertiary); andesite, alluvial and residual deposits (Quaternary)	Quartz, plagioclase, sericite, illite, calcite, propylite, argillic, silicification	< 17.0	Quartz: 240–320	Quartz: 0.2–6.2

2007). In the quartz-sulfide vein ores, the temperatures at Gunung Subang are 180–260 °C. This is identical to those measured at the Arinem Te- type epithermal deposit with 180–300 °C, 1–4 wt% NaCl. (Yuningsih et al., 2012), which is an epithermal deposit located in a Late Eocene-Early Miocene magmatic arc near Cianjur (Fig. 1b). Fluid inclusion evidence suggests that the ore mineralization most likely occurred at ~260 to 270 °C from fluid with a salinity of < 6.2 wt% NaCl, which can be deemed as a "high salinity"-type epithermal gold deposit.

According to the petrography of the fluid inclusions, there is some evidence of boiling. It can be seen that a slight increase in temperature (260–270 °C) and salinity (2.9–4.4 wt% NaCl.) is implied in the Salinity-Homogenization temperature diagram from the initial silicification to the quartz-sulfide vein (Fig. 15a). The coexistence of vapor-rich and liquid-rich inclusions (Fig. 11f) indicate that boiling may be an important process for the precipitation of precious and base metals in epithermal deposits (Watanabe, 1998), and that such an association of inclusions with different proportions of vapor and liquid phases is attributed to a heterogeneous environment resulting from boiling (Simmons et al., 2000). Degassing during the boiling process, of gasses such as H_2S and H_2Te, can promote the deposition of sulfide. Colloform banding texture was found (Fig. 4g), which is a significant textural indicator of good gold grades (Renato et al., 1995). Ismayanto et al. (2009) noticed bladed calcite in the Cicelak Vein. Studies on epithermal gold deposits and active geothermal systems show that bladed calcite is formed in a non-equilibrium supersaturated hydrothermal system and is crystallized directly from boiling solutions (Hedenquist and Browne, 1989; Hedenquist, 1990; Simmons and Christenson, 1994; Simmons and Browne, 2000).

As for the occurrence of Au, Lee and Kim (2003) discovered Au with the use of Atomic Absorption Spectrum (AAS), and Ismayanto et al. (2009) discovered granular gold in the host quartz of Cigadobras vein. In this study, Au is mainly found as telluride, with some telluride containing Ag, encapsulated in pyIII by way of SEM. Since there are similar geochemical parameters for Fe^{2+}, Co, and Ni in pyrite, Co and Ni are always found in pyrite crystal in the form of isomorphism. Therefore, the Co/Ni ratio in pyrite is significant in indicating the origin of the ore-forming fluid (Bralia et al., 1979). In this study, the Co/Ni at most tested points is greater than 1, ranging from 0.85 to 10.3 (except for Ni = 0), which indicates that the Au-bearing pyrite in Gunung Subang is mainly from magmatic hydrothermal.

According to the EPMA data of the three periods of pyrite, chalcopyrite, and sphalerite (Table 9), the relationships among Au-Ag and As-S are not obvious, indicating that trace elements play little role in the accumulation of Au. It is obvious that there are two types of pyrite: Au-bearing and that with no Au, suggesting that the distribution of Au is uneven in EPMA. BSE images show that the Au is mainly distributed in the fractures of crystals. However, the EPMA results for pyrite, combined with Reich et al. (2005), suggest that the gold in Gunung Subang can be in form of Au^0 (Fig. 16). There is a little Zn, Cu, and Co in the different periods of pyrite formation. The content of Au in pyrite varies significantly, with an Au/Ag ratio of 0.38–49, average 9.49.

The Au-Te ores are characterized by low As and Sb and elevated Pb and Zn contents, that is, with a low AsSb/PbZn ratio (Nikolaev et al., 2013), this may be the reason why there was no arsenopyrite observed in the ores. The thermodynamic stability conditions for Au and Ag-tellurides and native tellurium indicate an epithermal environment (Cook et al., 2009). Pyrite from low-sulfidation and alkaline igneous rock-hosted epithermal systems is enriched in Te (and Se) compared to pyrite from high-sulfidation epithermal and porphyry Cu deposits. Neutrality to alkaline fluids has the ability to effectively mobilize and transport Te. Fluid boiling in porphyry-epithermal systems can effectively precipitate Te in association with pyrite and Au (Keith et al., 2018).

Telluride mineralization is typical of many gold deposits in volcano plutonic belts of island-arc and greenstone types (Luo et al., 1999). Krennerite is the low-temperature (300 °C), low-pressure polymorph of $AuTe_2$ and higher temperatures and pressures favor the development of calaverite (Markham, 1960). Combined with results of fluid inclusions, the ore-forming temperature should be approximately 300 °C, otherwise Au_2Te would form. According to Yuningsih et al. (2014), the comparison of the geochemical composition of the Se-, Te-type deposits and Gunung Subang is shown in the Table 10.

7. Conclusions

The Gunung Subang gold deposit is an epithermal deposit related to volcanism that occurred during the Mid-Miocene (17.0 ± 0.4 Ma) in the Sunda Arc. The zircons can be divided into magmatic and inherited, and average $\varepsilon_{Hf}(t)$ value of magmatic zircons is 9.9 ± 0.64. It suggests that the arc magmatism has undergone primary contamination with juvenile crust and some also from ancient crust.

The sulfur isotopic and in-situ Pb isotopic composition of the sulfides and the discovery of Au-Ag-tellurides in the Gunung Subang gold deposit indicates that mineralization material is mainly related to Miocene to Pliocene volcanic rocks, and some mantle-derived materials may also be added.

Fluid inclusion data suggests that the ore mineralization most likely occurred at ~260 °C, from the fluid with a salinity of < 6.2 wt% NaCl. Boiling occurred through local mineralization. There is a weak trend of a decrease in temperature and salinity from pre-ore to late mineralization. The major Au-bearing minerals are krennerite, hessite and kurilite. The native gold (Au^0) may also exist in pyrite.

Acknowledgements

The research is financially supported by the National Natural Science Foundation of China (NSFC Nos. 41573039, U1603245, 41703051, and U1812402), Chinese Academy of Sciences "Light of West China" Program and Natural Science Foundation of Guizhou Province (No. [2018] 1171). Mr. Wijaya Lawrence and Mr. Haifeng Wang from PT. WILTON WAHANA INDONESIA company provided many supports for fieldtrips.

References

Afifi, A.M., Kelly, W.C., Essene, E.J., 1988. Phase relations among tellurides, sulphides, and oxides: II. Applications to telluride-bearing Ore Deposits. Econ. Geol. 83 (2), 395–404.
Alt, J.C., Burdett, J.W., 1992. Sulfur in Pacific deep-sea sediments (Leg 29) and implications for cycling of sediment in subduction zones. Proc. ODP Sci. Res. 129, 283–294.
Andersen, T., 2002. Correction of common lead in U-Pb analyses that do not report ^{204}Pb. Chem. Geol. 192, 59–79.
Angeles, A.C., Prihatmoko, S., Walker, J.S., 2002. Geology and alteration-mineralization characteristics of the Cibaliung epithermal gold deposit, Banten, Indonesia. Resour. Geol. 52, 329–339. https://doi.org/10.1111/j.1751-3928.2002.tb00143.x.
Bakker, R.J., Jansen, J.B.H., 1994. A mechanism for preferential H_2O leakage from fluid inclusions in quartz, based on TEM observations. Contrib. Miner. Petrol. 116 (1), 7–20.
Bao, Z.A., Chen, L., Zong, C., Yuan, H., Chen, K., Dai, M., 2017. Development of pressed sulfide powder tablets for in situ sulfur and lead isotope measurement using LA-MC-ICP-MS. Int. J. Mass Spectrom. 421, 255–262.
Basuki, A., Sumanagara, A.D., Sinambela, D., 1994. The Gunung Pongkor gold-silver deposit, West Java, Indonesia. J. Geochem. Explor. 50 (4), 91–142.
Blichert-Toft, J., Albaréde, F., 1997. The Lu-Hf isotope geochemistry of chondrites and the evolution of the mantle-crust system. Earth Planet. Sci. Lett. 148 (1–2), 243–258.
Bodnar, R.J., 1994. Revised equation and table for determining the freezing point depression of H,O-NaCl solutions. Sci. Comment 116 (1), 7–20.
Bralia, A., Sabatini, G., Troja, F., 1979. A revaluation of the Co/Ni ratio in pyrite as geochemical tool in ore genesis problems. Miner. Deposita 14, 353–374.
Carlile, J.C., Mitchell, A.H.G., 1994. Magmatic arcs and associated gold and copper mineralization in Indonesia. J. Geochem. Explor. 50, 91–142. https://doi.org/10.1016/0375-6742(94)90022-1.
Chen, Y.J., Pirajno, F., Wu, G., Qi, J.P., Xiong, X.L., 2011. Epithermal deposits in North Xinjiang, NW China. Int. J. Earth Sci. 101 (4), 889–917.
Cook, N.J., Ciobanu, C.L., Spry, P.G., Voudouris, P., the Participants of IGCP-486, 2009. Understanding gold-(silver)-telluride-(selenide) mineral deposits. Episodes 32 (4), 249–263.
Defant, M.J., Drummond, M.S., 1990. Derivation of some modern arc magmas by melting of young subducted lithosphere. Nature 347, 662–665.

Genna, A., Jébrak, M., Marcoux, E., Milési, J.P., 1996. Genesis of cockade breccias in the tectonic evolution of the Cirotan. Can. J. Earth Sci. 33 (1), 93–102.
Griffin, W., Pearson, N., Belousova, E., Jackson, S.V., Van Achterbergh, E., O'Reilly, S.Y., Shee, S., 2000. The Hf isotope composition of cratonic mantle: LA-MC-ICPMS analysis of zircon megacrysts in kimberlites. Geochim. Cosmochim. Acta 64 (1), 133–147.
Hall, R., 2002. Cenozoic geological and plate tectonic evolution of SE Asia and the SW Pacific _ computer-based reconstructions, model and animations. J. Asian Earth Sci. 20 (4), 353–431.
Hall, R., 2007. Cretaceous to late Miocene stratigraphic and tectonic evolution of West Java. Thirty-First. In: Annual Convention and Exhibition: Proceedings, Indonesian Petroleum Association, pp. 1–18.
Hall, R., Hattum, M.W.A.V., Spakman, W., 2008. Impact of India-Asia collision on SE Asia: the record in Borneo. Tectonophysics 451 (1–4), 366–389.
Hamilton, W., 1979. Tectonics of the Indonesian Region Washington. United States Government Printing Office.
Harijoko, A., Sanematsu, K., Duncan, R.A., Prihatmoko, S., Watanabe, K., 2004. Timing of the mineralization and volcanism at Cibaliung gold deposit, western Java, Indonesia. Resour. Geol. 54, 187–195.
Hedenquist, J.W., 1990. The thermal and geochemical structure of the Broadlands-Ohaaki geothermal system. Geothermics 19, 151–185.
Hedenquist, J.W., Arribas, A., Reynolds, T.J., 1998. Evolution of an intrusion-centered hydrothermal system: far Southeast-Lepanto porphyry and epithermal Cu-Au deposits, Pilippines. Econ. Geol. 93 (4), 373–404.
Hedenquist, J.W., Browne, P.R.L., 1989. The evolution of the Waiotapu geothermal system, New Zealand, based on the chemical and isotopic composition of its fluids, minerals and rocks. Geochim. Comochim. Acta 53, 2235–2257.
Heinrich, C.A., 2007. Fluid-fluid interactions in magmatic-hydrothermal ore formation. Rev. Mineral. Geochem. 65 (1), 363–387.
Heinrich, C.A., Driesner, T., Stefánsson, A., Seward, T.M., 2004. Magmatic vapor contraction and the transport of gold from the porphyry environment to epithermal ore deposits. Geology 32 (9), 761–764.
Hinrich, C.A., 2005. The physical and chemical evolution of low-salinity magmatic fluids at the porphyry to epithermal transition: a thermodynamic study. Miner. Deposita 39 (8), 864–889.
Hoog, J.C.M.D., Taylor, B.E., Bergen, M.J.V., 2001. Sulfur isotope systematics of basaltic lavas from Indonesia: implications for the sulfur cycle in subduction zones. Earth Planet. Sci. Lett. 189, 237–252.
Hu, Z., Liu, Y., Chen, L., Zhou, L., Li, M., Zong, K., Zhu, L., Ga, o.S., 2011. Contrasting matrix induced elemental fractionation in NIST SRM and rock glasses during laser ablation ICP-MS analysis at high spatial resolution. J. Anal. At. Spectrom. 26 (2), 425–430.
Hu, Z., Liu, Y., Gao, S., Liu, W., Zhang, W., Tong, X., Lin, L., Zong, K., Li, M., Chen, H., Zhou, L., Yang, L., 2012a. Improved in situ Hf isotope ratio analysis of zircon using newly designed X skimmer cone and jet sample cone in combination with the addition of nitrogen by laser ablation multiple collector ICP-MS. J. Anal. At. Spectrom. 27 (9).
Hu, Z., Liu, Y., Gao, S., Xiao, S., Zhao, L., Günther, D., Li, M., Zhang, W., Zong, K., 2012b. A "wire" signal smoothing device for laser ablation inductively coupled plasma mass spectrometry analysis. Spectrochim. Acta, Part B 78, 50–57.
Ismayanto, A.F., Syafrizal, Notosiswoyo, S., 2009. Mineralization horizon and structure control of epithermal system at Gunung Subang, Cianjur, West Java, Indonesia: implication for exploration. Int. Symp. Earth Sci. Technol.
Katili, J.A., 1974. Geological Environment of the Indonesian Mineral Deposits: A Plate Tectonic Approach. Direktorat Jenderal Pertambangan, Jakarta.
Katili, J.A., 1975. Volcanism and plate tectonics in the Indonesian island arcs. Tectonophysics 26, 165–188.
Kay, R.W., 1980. Volcanic arc magmas: Implications of a melting-mixing model for element recyling in the crust-upper mantle system. J. Geol. 88, 497–522.
Keith, M., Smith, D.J., Jenkin, G.R., Holwell, D.A., Dye, M.D., 2018. Areview of Te and Se systematics in hydrothermal pyrite from precious metal deposits: insights into ore-forming processes. Ore Geol. Rev. 96, 269–282.
Kim, I.J., Seo, J.R., Hong, S.S., Lee, J.H., Lee, S.R., Kim, B.C., Kee, W.S., Song, K.Y., 2002. Geological Survey of the Southern Part of the Bandung, Indonesia. KR-02(C)-07.
Lee, J.H., Kim, I.J., 2003. Geologic, fluid inclusion, and sulfur isotopic studies of hydrothermal deposit in the Tanggueng District, West Java, Indonesia. Econ. Environ. Geol. 36 (5), 321–328.
Li, Z.C., Li, Y.J., QI, J.H., Zhang, H.F., Yang, Z.Y., Liu, Z.B., Zhou, Y., 2016. Geochemical Characteristics and tectonic significance of the volcanic rocks from lower triassic huarui formation in West Qinling. Northwestern Geol. 49 (1), 26–33 Chinese with English abstract.
Li, X., Tang, G., Gong, B., Yang, Y., Hou, K., Hu, Z., Li, Q., Liu, Y., Li, W., 2013. Qinghu zircon: a working reference for microbeam analysis of U-Pb age and Hf and O isotopes. Chin. Sci. Bull. 58 (36), 4647–4654.
Liu, Y., Gao, S., Hu, Z., Gao, C., Zong, K., Wang, D., 2009. Continental and oceanic crust recycling-induced melt-peridotite interactions in the Trans-North China Orogen: U-Pb dating, Hf isotopes and trace elements in zircons from mantle xenoliths. J. Petrol. 51 (1–2), 537–571.
Liu, Y.S., Hu, Z., Zong, K.Q., 2010. Reappraisement and refinement of zircon U-Pb isotope and trace element analyses LA-ICP-MS. Chin. Sci. Bull. 55, 1535–1546.
Lu, H.Z., Fan, H., Ni, P., Ou, G.X., 2004. Shen K and Zhang W H. Fluid Inclusions. Beijing: Science Press, pp (in Chinese with English abstract).
Ludwig, K.R., 2003. User's manual for Isoplot 3.00 – A Geochronological Toolkit for Excel. Geochronology Center Special Publication, Berkeley, CA: Berkeley.
Luo, Z.K., Guan, K., Wang, M.Z., Wang, C.T., 1999. The features of telluride in some gold deposits, China. Gold Geol. 5 (3), 69–74 in Chinese with English abstract.
Mao, J.W., Li, Y.Q., 2001. Fluid inclusions of the Dongping gold telluride deposit in Hebei province, China: involvement of mantle fluid in metallogenesis. Miner. Deposits 20 (1), 23–36 Chinses with English abstract.
Marcoux, E., Milési, J.P., 1994. Epithermal gold deposits in West Java, Indonesia: geology, age and crustal source. J. Geochem. Explor. 50, 393–408.
Marcoux, E., Milési, J.P., Sohearto, S., Rinawan, R., 1993. Noteworthy mineralogy of the Au-Ag-Sn-W (Bi) epithermal ore deposit of Cirotan, West Java, Indonesia. Can. Mineral. 31 (3), 727–744.
Markham, N.L., 1960. Synthetic and natural phases in the system Au-Ag-Te. Econ. Geol. 55, 1148–1178.
Martin, H., 1999. Adakitic magmas: modern analogues of Archaean granitoids. Lithos 46, 411–429.
Maryono, A., Harrison, R.L., Cooke, D.R., Rompo, I., Hoschke, T.G., 2018. Technocis and geology of porphyry Cu-Au deposits along the eastern Sunda magmatic arc, Indonesia. Econ. Geoln 113 (1), 7–38.
Milési, J.P., Nehlig, P., Sunarya, Y., Sukandar, A., Felenc, J., 1994. Cirotan, West Java, Indonesia_ A 1.7 Ma Hybrid Epithermal Au-Ag-Sn-W Deposit. Econ. Geol. 89 (2), 227–245.
Milési, J.P., Marcoux, E., Sitorus, T., 1999. Pongkor (west Java, Indonesia), a pliocene supergene-enriched epithermal Au-Ag-(Mn) deposit. Miner. Deposita 34, 131–149.
Morris, J., Leeman, W., Tera, F., 1990. The subducted component in island arc lavas_ constraints from Be isotopes and B-Be systematics. Nature 344, 31–36.
Myo, M.T., Arifudin, I., Agung, H., Okki, V., Koichiro, W., 2014. Fluid Inclusion Studies of the Cijulang High-sulfidation Epithermal Prospect, West Java, Indonesia. In: 2014 3rd International Conference on Geological and Environmental Sciences. IACSIT Press, Singapore, pp. 55–59.
Nicholls, I.A., Harris, K.L., Taylor, S.R., 1980. Variation in the geochemistry of mantle sources for tholtiitic and calc-alkaline mafic magmas, Wwstern Sunda volcanic arc, Indonesia. Chem. Geol. 30, 177–199.
Nikolaev, YuN., Prokof'ev, V.Yu, Apletalin, A.V., Vlasov, E.A., Baksheev, I.A., Kal'ko, I.A., Komarova, Ya.S., 2013. Gold–telluride mineralization of the Western Chukchi Peninsula, Russia: mineralogy, geochemistry, and formation conditions. Geol. Ore Deposits 55, 114–144.
Perfit, M., Gust, D., Bence, A.E., Arculus, R., Taylor, S.R., 1980. Chemical characteristics of island.
Plank, T., Langmuir, C.H., 1993. Tracing trace elements from sediment input to volcanic output at subduction zones. Nature 362, 739–743.
Qi, L., Hu, J., Gregoire, D.C., 2000. Determination of trace elements in granites by inductively coupled plasma mass spectrometry. Talanta 51, 507–513.
Reich, M., Kesler, S.E., Utsunomiya, S., Palenik, C.S., Chryssoulis, S.L., Ewing, R.C., 2005. Solubility of gold in arsenian pyrite. Geochim. Cosmochim. Acta 69 (11), 2781–2796.
Renato, E., Bobis, S.J., Gregg Morrison, W., 1995. The anatomy of a Carboniferous epithermal ore shoot at Pajingo, Queensland Setting, zoning, alteration, and fluid conditions. Econ. Geol. 90, 1776–1798.
Richards, J.P., 2009. Postsubduction porphyry Cu-Au and epithermal Au deposits: products of remelting of subduction-modified lithosphere. Geology 37 (3), 247–250.
Rosana, M.F., Matsueda, H., 2002. Cikidang hydrothermal gold deposit in Western Java, Indonesia. Resour. Geol. 52 (4), 341–352.
Rudnick, R.L., Gao, S., 2003. Composit ion of the cont inental crust. Treatise on geochemistry, pp. 1–64.
Sakai, H., Des Marais, D.J., Ueda, A., Morre, J.G., 1984. Concentrations and isotope ratios of carbon, nitrogen and sulfur in ocean-floor basalts. Geochim. Cosmochim. Acta 48, 2433–2441.
Setijadji, L.D., Kajino, S., Imai, A., Watanabe, K., 2006. Cenozoic Island Arc Magmatism in Java Island (Sunda Arc, Indonesia) Clues on Relationships between Geodynamics of Volcanic Centers and Ore Mineralization. Resour. Geol. 56 (3), 267–292.
Sigmarsson, O., Condomines, M., Morris, J., Harmon, R., 1990. Uranium and ^{10}Be enrichments by fluids in Andean arc magmas. Nature 346, 163–165.
Simmons, S.F., Arehart, G., Simpson, M.P., Mauk, J.L., 2000. Origin of massive calcite veins in the Golden Cross low-sulfidation, epithermal Au-Ag deposit, New Zealand. Econ. Geol. 95, 99–112.
Simmons, S.F., Browne, P.R.L., 2000. Hydrothermal minerals and precious metals in the Broadlands-Ohaaki geothermal system: implications for understanding low-sulfidation epithermal environments. Econ. Geol. 95, 971–1000.
Simmons, S.F., Christenson, B.W., 1994. Origins of calcite in a boiling geothermal system. Am. J. Sci. 294, 361–400.
Söderlund, U., Patchett, P.J., Vervoort, J.D., Isachsen, C.E., 2004. The ^{176}Lu decay constant determined by Lu-Hf and U-Pb isotope systematics of Precambrian mafic intrusions. Earth Planet. Sci. Lett. 219 (3), 311–324.
Soeria, A.R., Maury, R.C., Bellon, H., Pringgoprawiro, H., Polve, M., Priadi, B., 1994. Tertiary magmatic belts in Java. J. SE Asian Earth Sci. 9 (1–2), 13–27.
Soreia, A.R., Maury, R.C., Pringgoprawiro, H.B., Priadit, M.P., 1994. Tertiary magmatic belts in Java. J. Southeast Asian Earth Sci. 9, 13–27.
Stacey, J.S., 1975. Approximation of terrestrial lead isotope evolution by a two-stage model. Earth Planet. Sci. Lett. 26, 207–221.
Sudana, D., Santosa, S., 1992. Geology of the Cikarang Quadrangle, Java. Scale 1: 100. 000. Geological Research and Development cemter, pp. 13.
Sun, S.S., McDonough, W.F., 1989. Chemical and isotopic systematics of oceanic basalts: implications for mantle composition and processes. Geol. Soc., London, Spec. Public. 42 (1), 313–345.
Van, B.R.W., 1970. The Geology of Indonesia: The Hague. Martinus Nijhoff, pp. 732.
Wagner, T., Williams-Jones, A.E., Boyce, A.J., 2005. Stable isotope-based modeling of the origin and genesis of an unusual Au-Ag-n-W epithermal system at Cirotan, Indonesia. Chem. Geol. 219, 237–260.
Wakita, K., Metcalfe, I., 2005. Ocean plate stratigraphy in east and southeast Asia. J. Asian Earth Sci. 24 (6), 679–702.
Watanabe, A., 1998. "Extreme boiling" model for variable salinity of the Hokko low-

sulfidation epithermal Au prospect, southwestern Hokkaido, Japan. Miner. Deposita 33, 568–578.
Widi, B.N., Matsueda, H., 1998. Epithermal gold-silver-tellurides-deposit of Cineam, Tasikmalaya District, West Java, Indonesia. Directorate of Mineral Resources Indonesia, Special Publication, pp. 1–19.
Widjaja, W., 2017. Short information memorandum farmin, financing & developing of gold mine joint ventures (JV) companies.
Winchester, J.A., Floyd, P.A., 1977. Geochemical discrimination of different magma series and their differentiation products using immobile elements. Chem. Geol. 20, 325–343.
Wu, C.Q., Zhang, Z.W., Zheng, C.F., Yao, J.H., 2014. Mid-Miocene (~17 Ma) quartz diorite porphyry in Ciemas, West Java, Indonesia, and its geological significance. Int. Geol. Rev. 57 (9–10), 1294–1304.
Wu, C.Q., Zhang, Z.W., Rosana, M.F., Shu, Q., Zheng, C.F., Xu, J.H., Li, X.Y., Jin, Z.R., 2019. The continental crust contributes to magmatic hydrothermal gold deposit in Ciemas, West Java, Indonesia: Constrains from Hf isotopes of zircons and *in situ* Pb isotopes of sulphides. Ore Geol. Rev., 103010.
Yuan, H., Liu, X., Chen, L., Bao, Z.A., Chen, K., Zong, C., Li, X.C., Qiu, J.W., 2018. Simultaneous measurement of sulfur and lead isotopes in sulfides using nanosecond laser ablation coupled with two multi-collector inductively coupled plasma mass spectrometers. J. Asian Earth Sci. 154, 386–396.
Yuningsih, E.T., Hiroharu, Matsueda, Setyaraharja, Eko, P., Rosana, M.F., 2012. The Arinem Te-bearing gold-silver-base metal deposit, West Java, Indonesia. Resour. Geol. 62 (2), 140–158.
Yuningsih, E.T., Matsueda, H., Rosana, M.F., 2014. Epithermal gold-silver deposits in Western Java, Indonesia: gold-silver selenide-telluride mineralization. Indonesian J. Geosci. 1 (2), 71–81.
Zhang, Z.W., Wu, C.Q., Yang, X.Y., Zheng, C.F., Yao, J.H., 2015. The trinity pattern of Au deposits with porphyry, quartz–sulfide vein and structurally-controlled alteration rocks in Ciemas, West Java, Indonesia. Ore Geol. Rev. 64, 152–171.
Zheng, C.F., Zhang, Z.W., Wu, C.Q., Yao, J.H., 2015. Geochemical Characteristics of Sulfur Isotopes and Trace Elements in the Ciemas Gold Mine, West Java, Indonesia. Bull. Mineral., Petrol. Geochem. 34 (4), 812–819 Chinese with English abstract.
Zheng, C.F., Zhang, Z.W., Wu, C.Q., Yao, J.H., 2017. Genesis of the Ciemas Gold Deposit and Relationship with Epithermal deposits in West Java, Indonesia: constraints from fluid inclusions and stable isotopes. Acta Geol. Sin. (English Edition) 91 (3), 801–840.
Zhou, Q.F., Li, S.R., Chen, H.Y., Song, Y.B., Zhang, X.B., Cui, J.C., 2011. Discovery and geological significance of telluride minerals in the Yinggezhuang gold deposit, Rushan, Jiaodong. Acta Petrol. Sin. 27 (6), 1847–1856 Chinese with English abstract.